NISSUNA UMANA INVESTIGAZIONE SI PUO DIMANDARE VERA SCIENZIA
S'ESSA NON PASSA PER LE MATEMATICHE DIMOSTRAZIONI
LEONARDO DA VINCI

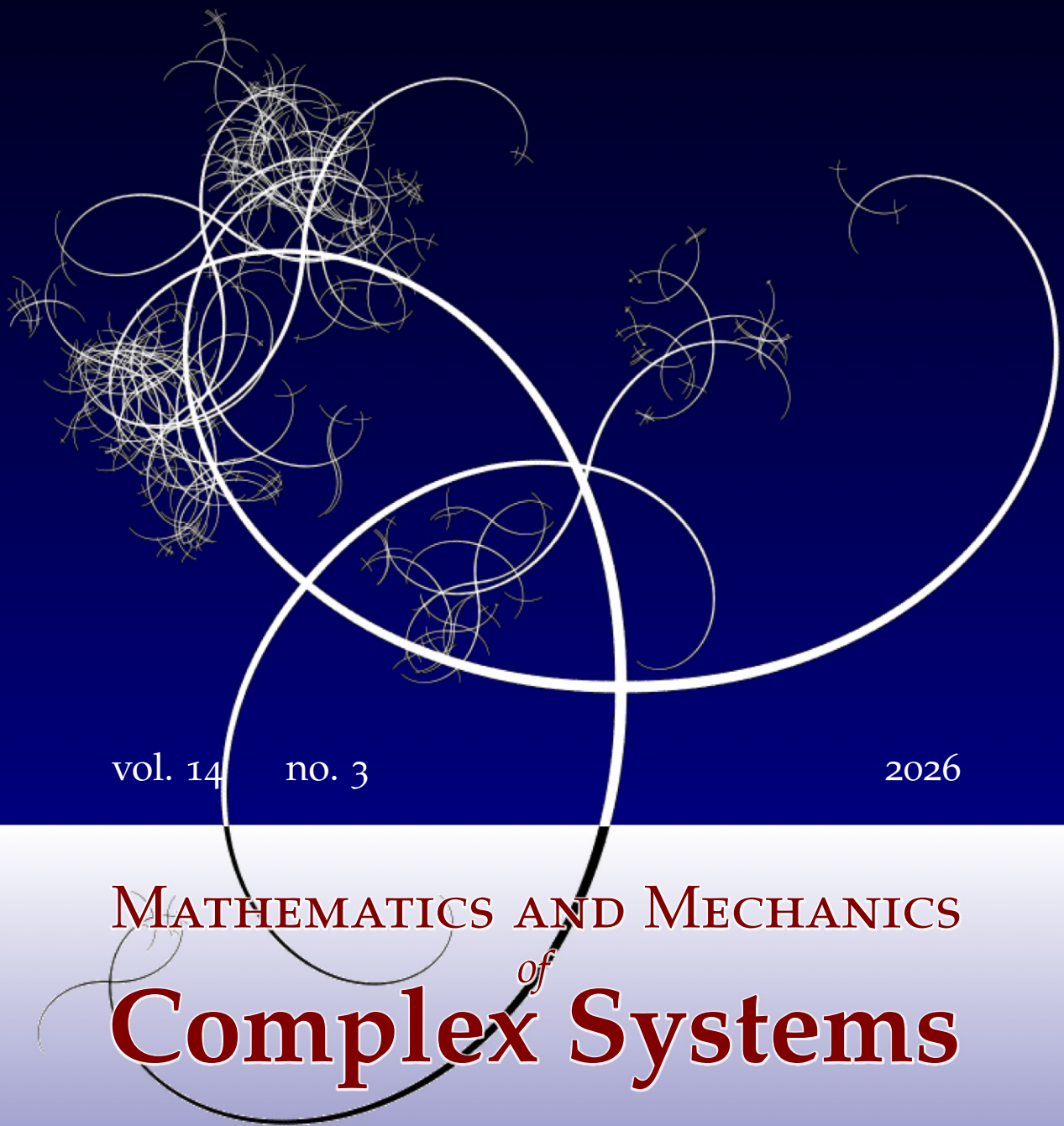

vol. 14 no. 3 2026

Mathematics and Mechanics *of* Complex Systems

EMILIO BARCHIESI

ELASTIC RAREFACTION SOLITARY WAVES IN MONOLAYERED PANTOGRAPHIC WAVEGUIDES WITH NEARLY INEXTENSIBLE LINKS VERIFIED BY DISCRETE MICROMODELING

msp

MATHEMATICS AND MECHANICS OF COMPLEX SYSTEMS
Vol. 14 (2026), No. 3, pp. 309–339
DOI: 10.2140/memocs.2026.14.309

ELASTIC RAREFACTION SOLITARY WAVES IN MONOLAYERED PANTOGRAPHIC WAVEGUIDES WITH NEARLY INEXTENSIBLE LINKS VERIFIED BY DISCRETE MICROMODELING

EMILIO BARCHIESI

This study demonstrates, via a homogenized continuum model, that monolayered pantographic waveguides with nearly inextensible flexural elements support the propagation of rarefaction solitary waves, whose crests correspond to complete cell closure. To validate the continuum approach and explore key parametric effects, time-dependent simulations are conducted at a discrete scale examining the influence of the total number of cells, the applied displacement rate, and the extensional stiffness of the flexural elements on solitary wave propagation. The interaction of solitary waves is also investigated. Results reveal that, for an odd number of cells, the solitary waves emerge from the collision relatively unaltered, whereas for an even number of cells, the region between the two crests experiences extreme compression, culminating in complete cell closure and the formation of two propagating tails.

1. Introduction

Solitons are defined as localized wave solutions to nonlinear differential equations that preserve their shape and velocity, and emerge unchanged, except for a phase shift, after collisions [31]. When such waves lack this collision property, they are referred to as solitary waves. These typically arise from nonlinear, reversible interactions described by partial differential equations such as the Korteweg–de Vries equation for shallow water waves [52], the nonlinear Schrödinger equation for light in optical fibers and Bose–Einstein condensates [14; 57], and the sine-Gordon equation, used in modeling Josephson junctions and crystal dislocations [50; 61]. Mathematically, traveling waves of permanent form with compact support can arise due to either strong nonlinearities (beyond quadratic) in higher-order gradient terms or specific inhomogeneities in quadratic gradient terms [18]. Solitary waves may also occur in dissipative systems, such as those governed by the Burgers equation. In their seminal work, Zabusky and Kruskal [77] linked the Fermi–Pasta–Ulam–Tsingou problem [43] to solitons by showing that, under certain conditions, it approximates solutions to the Korteweg–de Vries equation.

The recent advancements and increasing accessibility of 3D printing have stimulated significant interest in mechanical metamaterials. Owing to their engineered microstructures, these materials exhibit unconventional properties absent in classical materials. Local deformations and rotations [20; 34; 35; 36], as well as nonrigid zero-energy modes [2; 3; 32], have been identified as key mechanisms underlying such behaviors, which are effectively described by higher-gradient [1], micromorphic [12; 46; 48; 58; 59; 62],

Communicated by Francesco dell'Isola.
MSC2020: 74Q05, 74S99.
Keywords: solitary waves, pantographic waveguides, homogenization, Weierstrass' analysis, discrete modeling.

and nonlocal theories [9; 10; 11; 56]. Among the higher-gradient theories one finds three-dimensional higher-gradient models [26; 40; 51] and their geometrically reduced counterparts, such as higher-order plate and shell [6; 16; 65; 66], membrane [49; 63; 64], beam and rod theories [54; 60]. Micromorphic theories include micropolar models [4; 15; 35]. These generalized continuum theories pose notable challenges, particularly in extending the classical notion of Cauchy stress [27; 38]. As an instance, in second-gradient continua, the internal virtual work depends on both first and second gradients of the virtual displacement, leading to the definition of Piola–Lagrange and Cauchy–Euler stresses, as well as a third-order double-stress tensor. Formulating these models necessitates the use of modern differential geometry, wherein deformations are treated as diffeomorphisms between Riemannian embedded submanifolds [41; 42]. Metamaterials are capable of exhibiting unique nonlinear static and dynamic responses, making them ideal candidates for a wide range of advanced applications [19; 53; 69; 75; 76]. A notable example of emergent macroscale behavior is found in deployable metamaterials, such as origami-inspired and pantographic structures, where the existence of nonrigid zero-energy modes enables extreme compliance over large elastic deformations, followed by stiffening associated with full opening or closure [28; 29]. Fraternali et al. [21; 44] studied lattices of masses connected by tensegrity prisms, revealing two distinct dynamic regimes: a low-energy (sonic) regime where solitary waves with sech^2 profiles propagate, and a high-energy (ultrasonic) regime characterized by atomic-scale localization. Numerical studies demonstrated that such systems, in 1D–3D configurations, can be tuned between elastic hardening and softening regimes via prestress. In the softening regime, an initial compression pulse transforms into a solitary rarefaction wave followed by a decaying oscillatory tail. A waveguide is a structure that channels wave propagation by constraining energy transmission to a single spatial direction. Pantographic waveguides are mechanical systems composed of flexible elements hinge-connected in a diamond-shaped pattern. The dynamic response of pantographic metamaterials has been investigated numerically through both continuum and discrete models [55; 70; 71], though only a few studies have specifically addressed the propagation of solitary waves, providing important insights and methodologies but without definitive conclusions [17; 37; 73].

Monolayered pantographic waveguides can store elastic energy associated with stretch gradients [7] and exhibit rotary inertia effects [33], resulting in unusual dispersion characteristics [8; 68]. These features support the hypothesis that solitary waves may propagate in such structures. An initial numerical investigation of this phenomenon, based on a continuum approach and time-dependent finite element simulations, was conducted by Giorgio et al. [47], introducing cubic nonlinearity into a one-dimensional model in the small deformation regime. Differently from the work Giorgio et al., the present study employs a homogenized continuum model, based on Hookean interaction potentials at the microscale, where flexural elements are treated as quasi-inextensible and the formulation remains valid in the large deformation regime. Conditions for the admissibility of solitary wave propagation in monolayered pantographic waveguides are derived analytically. A qualitative analysis of the continuum equations shows that the system supports rarefaction-type elastic solitary waves with noncompact support and, subsequently, solitary waveforms are computed numerically. To validate the continuum model and investigate key

parametric influences, detailed time-dependent simulations of the corresponding discrete system are performed. In particular, the effects of the total number of cells, the applied displacement rate, and the extensional stiffness of the flexural elements on solitary wave propagation are examined. The interaction of solitary waves is also analyzed: for an odd number of cells, solitary waves emerge from collisions largely unaltered, while for an even number of cells, the region between the wave crests undergoes extreme compression, leading to complete cell closure and the generation of two propagating tails.

2. Discrete and continuum modeling

A discrete mechanical system is introduced at the microscale, with its geometry and lumped elastic elements shown in the undeformed configuration in Figure 1 (top). The system exhibits periodicity and consists of N identical cells arranged along a straight line in the direction of the unit basis vector $\boldsymbol{e}_x$, resulting in a total longitudinal length L. The cells are centered at positions $P_i = i\varepsilon$, for $i \in \{0, 1, \ldots, N\}$, where $\varepsilon = L/N$. Hinge constraints are represented by white-filled circles. Each basic cell is composed of four oblique bars, assumed at this stage to be arbitrarily deformable along their axial direction, and hinge-connected at the point P_i. Flexural stiffness is introduced via rotational springs, shown in green and red in Figure 1 (top) placed between opposite oblique bars of the same cell. While more sophisticated modeling of the flexural elements could be considered at the microscale, this simplified representation is adopted for clarity and tractability. Extensional springs are placed between adjacent nodes along the centerline of the monolayered pantographic waveguide. These nodes are constrained to move exclusively along the axial direction $\boldsymbol{e}_x$. The motion of the entire system is confined to the plane, and due to its symmetry and constraints of the centerline nodes, since only points lying on the centerline are considered to be accessible from the external world, all deformed configurations remain symmetric with respect to the centerline, as depicted in Figure 1 (bottom). The same figure also introduces the kinematic quantities that will be used throughout the manuscript.

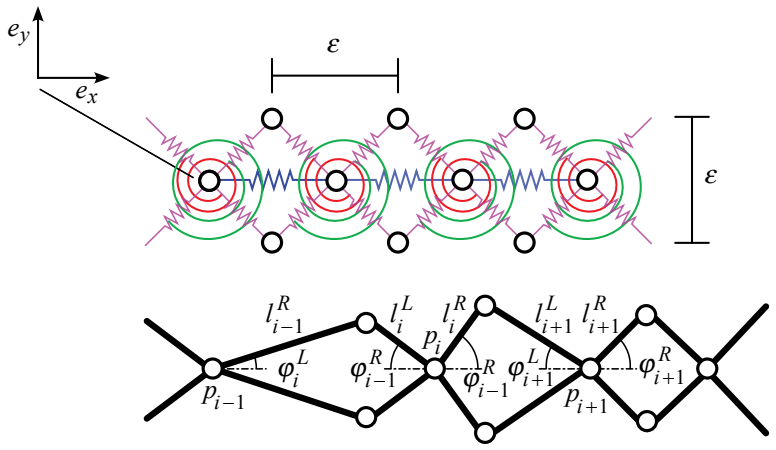

Figure 1. Top: geometry and lumped elastic elements of the discrete system in the undeformed configuration. Bottom: deformed configuration and kinematic quantities of the discrete system.

When not otherwise mentioned, the indices i and ν belong henceforth to the index sets $i \in \{0, 1, \dots, N\}$ and $\nu \in \{L, R\}$, respectively. It is worth to mention that the kinematics of the discrete system is locally described by finitely many generalized coordinates. As an instance, such coordinates can be chosen as the current positions p_i along the centerline of the points at positions P_i in the reference configuration and the lengths of the oblique (deformed) bars at the left and right of the central hinges, denoted as l_i^ν or, alternatively to l_i^ν, the angles φ_i^ν; see Figure 1 (bottom). To prevent any square cell in the microstructure collapsing into a horizontal or a vertical segment, it is assumed that the angle φ_i^ν remains in the range $(0, \pi/2)$. Applying the law of cosines, the two choices for the generalized coordinates can be related as follows:

$$\begin{aligned} \varphi_i^R &= \cos^{-1}\left[\frac{(p_{i+1}-p_i)^2 + (l_i^R)^2 - (l_{i+1}^L)^2}{2l_i^R(p_{i+1}-p_i)}\right], \\ \varphi_i^L &= \cos^{-1}\left[\frac{(p_i-p_{i-1})^2 + (l_i^L)^2 - (l_{i-1}^R)^2}{2l_i^L(p_i-p_{i-1})}\right]. \end{aligned} \tag{1}$$

Note that φ_0^ν and φ_N^ν cannot be determined by the relations (1) and, strictly speaking, belong also to the set of generalized coordinates. However, for the sake of brevity they will often be omitted. The deviation angle of two opposite oblique springs from lying on the same line is given for the entire index set of i by

$$\beta_i = \varphi_i^R - \varphi_i^L. \tag{2}$$

It is now possible to define the micromodel deformation energy as

$$\mathcal{U}_\varepsilon = \mathcal{E}_\varepsilon = k_E \sum_i \sum_\nu \left(l_i^\nu - \frac{\sqrt{2}}{2}\varepsilon\right)^2 + k_F \sum_i \beta_i^2 + \frac{k_S}{2} \sum_i (p_{i+1} - p_i - \varepsilon)^2 \tag{3}$$

with $k_E, k_F, k_S \geq 0$ being the stiffnesses of the bars (colored in magenta in Figure 1 (top)), of the rotational springs, and of the extensional springs (colored in blue), respectively, which are assumed to not depend on the index i. It is worth remarking that, when extensional springs have vanishing stiffness k_S, besides the rigid body modes, also the set of configurations defined by

$$p_i = p_{i-1} + K, \quad p_0 = P_0, \quad l_i^\nu = \frac{\sqrt{2}}{2}\varepsilon \qquad \text{for } K \in (0, \sqrt{2}\varepsilon), \tag{4}$$

which corresponds to a homogeneous elongation/compression in the characteristic scissor-like pattern along the longitudinal direction, yields a null deformation energy [3].

The asymptotic homogenization with respect to ε of the microstructure introduced above is now addressed. It is assumed that the extensible bars have a length which, at leading order, is proportional to ε, when $\varepsilon \to 0$,

$$l_i^\nu = \frac{\sqrt{2}}{2}\varepsilon + \varepsilon^2 \tilde{l}_i^\nu + o(\varepsilon^2), \tag{5}$$

where $\tilde{l}_i^\nu \in \mathbb{R}$. The sought continuum is assumed to be one-dimensional and to be parametrized by the arclength $s \in [0, L]$ of the straight segment of length L connecting all points P_i. It is assumed that the placement function $\chi : [0, L] \to \mathbb{R}$ and the microstretches $\tilde{l}^\nu$ are the independent kinematic Lagrangian

fields of the macromodel. Inserting assumption (5) into the deformation energy of the discrete system leads to

$$\mathcal{U}_\varepsilon = k_E \sum_i \sum_\nu [\varepsilon^2 \tilde{l}_i^\nu + o(\varepsilon^2)]^2 + k_F \sum_i (\beta_i)^2 + \frac{k_S}{2} \sum_i (p_{i+1} - p_i - \varepsilon)^2. \tag{6}$$

The micro-macro identification relating the generalized coordinates of the discrete system with the functions χ and $\tilde{l}_i^\nu$ is performed by considering the condition $\chi(s_i) = p_i$ and $\tilde{l}^\nu(s_i) = \tilde{l}_i^\nu$, where $s_i = i\varepsilon$. The discrete deformation energy is further expanded in ε expanding the field χ as

$$\chi(s_{i\pm1}) = \chi(s_i) \pm \varepsilon \chi'(s_i) + \frac{\varepsilon^2}{2} \chi''(s_i) + o(\varepsilon^2), \tag{7}$$

where prime denotes differentiation with respect to s. The difference between the positions of two adjacent points in the current configuration is computed as

$$p_{i+1} - p_i = \varepsilon \left[\chi'(s_i) + \frac{\varepsilon}{2} \chi''(s_i) + o(\varepsilon) \right] \quad \text{and} \quad p_i - p_{i-1} = \varepsilon \left[\chi'(s_i) - \frac{\varepsilon}{2} \chi''(s_i) + o(\varepsilon) \right]. \tag{8}$$

The expansion of the term β_i with respect to ε is now sought. Let us define $h(\varepsilon)$ as the argument of one of the functions $\cos^{-1}$ in (1). The expansions (8) and (5) are substituted into $h(\varepsilon)$ and, recalling that the angle φ_i^ν can be expanded as

$$\cos^{-1}[h(0)] - \frac{\varepsilon}{\sqrt{1 - h(0)^2}} h'(0) + o(\varepsilon), \tag{9}$$

leading to

$$\beta_i = \left. \frac{2\chi'(\tilde{l}^R - \tilde{l}^L) - \sqrt{2}\chi''}{\sqrt{2}\sqrt{2 - \chi'^2}} \right|_{s=s_i} \varepsilon + o(\varepsilon), \tag{10}$$

which is well defined only if $0 < \chi'(s_i) < \sqrt{2}$, namely if each square cell in the microstructure does not collapse into a horizontal or vertical segment. The desired expansion of the micromodel energy $\mathcal{U}_\varepsilon$ as a function of the fields χ and $\tilde{l}^\nu$ hence reads as

$$\mathcal{U}_\varepsilon = \varepsilon^2 \left\{ k_E \varepsilon^2 \sum_i \sum_\nu [(\tilde{l}_i^\nu)^2 + o(\varepsilon^0)] + k_F \sum_i \left[\left. \frac{2\chi'(\tilde{l}^R - \tilde{l}^L) - \sqrt{2}\chi''}{\sqrt{2}\sqrt{2 - \chi'^2}} \right|_{s=s_i} + o(\varepsilon^0) \right]^2 \right.$$
$$\left. + \frac{k_S}{2} \sum_i [\chi'(s_i) - 1 + o(\varepsilon^0)]^2 \right\}. \tag{11}$$

Let the parameters $K_E, K_F, K_S > 0$ be independent of ε. The parameters k_E, k_F, and k_S are related to ε by the scaling laws

$$k_E = K_E \varepsilon^{-3}, \quad k_F = K_F \varepsilon^{-1}, \quad k_S = K_S \varepsilon^{-1} \tag{12}$$

acting on the family of discrete models parametrized on ε, and the continuum limit of the deformation energy is obtained by letting $\varepsilon \to 0$:

$$\mathcal{U} = \int_0^L \left\{ \sum_\nu K_E (\tilde{l}_i^\nu)^2 + K_F \left[\frac{2\chi'(\tilde{l}^R - \tilde{l}^L) - \sqrt{2}\chi''}{\sqrt{2}\sqrt{2 - \chi'^2}} \right]^2 + K_S (\chi' - 1)^2 \right\} \mathrm{d}s. \tag{13}$$

The kinetic energy conveyed by the oblique bars shall now be addressed. The kinetic energy of a deformable bar is postulated to have the form (compare [13, page 210, equation (17.48)])

$$K_{BAR} = \frac{m_B}{2}\left\|\frac{\dot r_1+\dot r_2}{2}\right\|^2 + \frac{i_B}{2}\|\dot r_2-\dot r_1\|^2,$$

where r_1 and r_2 denote the positions of its two endpoints. For the right and left bars of the i-th unit cell one has

$$\frac{\dot r_1+\dot r_2}{2} = \dot p_i e_x + \frac{1}{2}(l_i^{R(S)}\dot\varphi_i^{R(S)}\hat t + \dot l_i^{R(S)}\hat n) \quad \text{and} \quad \dot r_2-\dot r_1 = l_i^{R(S)}\dot\varphi_i^{R(S)}\hat n + \dot l_i^{R(S)}\hat t,$$

where $\hat t$ denotes the unit vector directed from r_1 to r_2 and $\hat n$ denotes the unit vector obtained by rotating $\hat t$ in the counterclockwise direction by 90°. Note that, at the leading order in ε, if $o(\varepsilon^0)$ terms are neglected, then

$$\varphi_i^R = \varphi_i^S = \cos^{-1}\left(\frac{\chi'}{\sqrt2}\right)\Big|_{s=s_i},$$

while the term $l_i^{R(S)}\dot\varphi_i^{R(S)}$, taking into account (5), reads at the leading order in ε as

$$\frac{\sqrt2\varepsilon}{2}\frac{\mathrm d}{\mathrm dt}\left[\cos^{-1}\left(\frac{\chi'}{\sqrt2}\right)\right]_{s=s_i}$$

and the term $\dot l_i^{R(S)}$ reads as $\varepsilon^2\frac{\mathrm d}{\mathrm dt}\tilde l_i^{\nu}$. Therefore, at leading order in ε, for the left and right bars of the i-th unit cell one has

$$\frac{\dot r_1+\dot r_2}{2} = \dot p_i \quad \text{and} \quad \dot r_2-\dot r_1 = \frac{\sqrt2\varepsilon}{2}\frac{\mathrm d}{\mathrm dt}\left[\cos^{-1}\left(\frac{\chi'}{\sqrt2}\right)\right]_{s=s_i}.$$

The kinetic energy of the discrete system hence reads, up to higher order terms in ε, as

$$\mathcal K_\varepsilon = 2m_B\sum_i \dot p_i^2 + \sqrt2 i_B\varepsilon\sum_i\left[\frac{\mathrm d}{\mathrm dt}\cos^{-1}\left(\frac{\chi'}{\sqrt2}\right)\right]^2_{s=s_i},$$

leading at the continuum, considering the scaling laws $m_B = M_B\varepsilon$ and $i_B = I_B$, where M_B and I_B are two positive reals that do not depend upon ε, to

$$\mathcal K = \int_0^L\left[2M_B\dot\chi^2 + \sqrt2 I_B\left(\frac{-1}{\sqrt2\sqrt{1-\chi'^2/2}}\frac{\mathrm d\chi'}{\mathrm dt}\right)^2\right]\mathrm ds.$$

Having derived the Lagrangian of the continuum, it is now possible to compute its first variation with respect to $\tilde l^{\nu}$ to perform a static condensation (note that the kinetic energy density of the continuum does not depend on $\tilde l^{\nu}$ and that the deformation energy density depends only algebraically on $\tilde l^{\nu}$). Introducing the displacement field $u(s) = \chi(s) - s\boldsymbol e_x$, this results in a linear system of two equations in the unknowns $\tilde l^{\nu}$, giving

$$\tilde l^R = -\tilde l^L = \frac{\sqrt2 K_F(1+u')u''}{4K_F[(1+u')^2-2]-K_E(1+u')^2}. \tag{14}$$

Note that, according to the last equality, at the continuum scale, the elongation of the right and left oblique bars tends, as expected, to zero as K_E tends to infinity. Additionally, at each point, the compression

(extension) of the left bars is equal to the extension (compression) of the right bars and their deformation does not depend on K_S. By substituting the statically condensed microstretches (14) back into the continuum deformation energy density, the Lagrangian function of the considered monolayered pantographic waveguide reads, in terms of the displacement field, as

$$\mathcal{L} = \mathcal{U} - \mathcal{K} \tag{15}$$

$$= \int_0^L \left[\frac{K_E K_F (1+u')^2}{[2-(1+u')^2][(1+u')^2(K_E-4K_F)+8K_F]} u''^2 + K_S u'^2 - 2M_B \dot{u}^2 - \frac{\sqrt{2} I_B}{2-(1+u')^2} \left(\frac{\mathrm{d}u'}{\mathrm{d}t} \right)^2 \right] \mathrm{d}s. \tag{16}$$

It is worth emphasizing that the earlier assumption, that no square cell in the microstructure collapses into a horizontal or vertical segment, can be reformulated in terms of the displacement field as $0 < 1+u' < \sqrt{2}$. Moreover, the upper bound $1+u' < \sqrt{2}$ must hold almost everywhere (i.e., except possibly at isolated points) to ensure the well-posedness of the Lagrangian formulation introduced above.

3. Admissibility of solitary waves

To begin with, an infinitely long waveguide is considered, with the abscissa s spanning the entire real line, i.e., $s \in [-\infty, +\infty]$. Traveling wave solutions are sought such that

$$u(x,t) = \tilde{u}(\xi), \tag{17}$$

where $\xi = s - ct$ is the phase variable, with $c \in \mathbb{R}$ being the wave velocity, independent of s and t. Plugging the sought solutions into the Lagrangian above gives

$$\mathcal{L} = \int_{-\infty}^{+\infty} \left[\left\{ \frac{K_E K_F \left(1+\frac{\mathrm{d}\tilde{u}}{\mathrm{d}\xi}\right)^2}{\left[\left(1+\frac{\mathrm{d}\tilde{u}}{\mathrm{d}\xi}\right)^2 (K_E-4K_F)+8K_F\right]} - \sqrt{2}c^2 I_B \right\} \frac{\left(\frac{\mathrm{d}^2\tilde{u}}{\mathrm{d}\xi^2}\right)^2}{2-\left(1+\frac{\mathrm{d}\tilde{u}}{\mathrm{d}\xi}\right)^2} + (K_S - 2c^2 M_B) \left(\frac{\mathrm{d}\tilde{u}}{\mathrm{d}\xi} \right)^2 \right] \mathrm{d}\xi. \tag{18}$$

The least action principle, which considers admissible variations δu depending on s and t only through the variable ξ, namely $\delta u(s,t) = \delta\tilde{u}(s-ct)$, leads to (see the Appendix for more details)

$$\frac{\mathrm{d}^2\tilde{u}}{\mathrm{d}\xi^2} \left(\frac{\partial \mathscr{L}}{\partial\left(\frac{\mathrm{d}^2\tilde{u}}{\mathrm{d}\xi^2}\right)} \right) - \mathscr{L} - \gamma \frac{\mathrm{d}\tilde{u}}{\mathrm{d}\xi} = \eta, \tag{19}$$

where $\mathscr{L}$ is the Lagrangean density. Plugging the expression in (18) for the Lagrangean density $\mathscr{L}$ into the last equality, performing the position $v = \frac{\mathrm{d}\tilde{u}}{\mathrm{d}\xi}$ gives

$$\left\{ \frac{K_E K_F (1+v)^2}{[(1+v)^2(K_E-4K_F)+8K_F]} - \sqrt{2}c^2 I_B \right\} \frac{\left(\frac{\mathrm{d}v}{\mathrm{d}\xi}\right)^2}{2-(1+v)^2} - (K_S - 2c^2 M_B) v^2 - \gamma v = \eta, \tag{20}$$

which, dividing both sides by

$$\frac{1}{2-(1+v)^2} \left\{ \frac{K_E K_F (1+v)^2}{[(1+v)^2(K_E-4K_F)+8K_F]} - \sqrt{2}c^2 I_B \right\},$$

can be rewritten as

$$\left(\frac{\mathrm{d}v}{\mathrm{d}\xi}\right)^2 + \frac{[(K_S - 2c^2M_B)v^2 + \gamma v + \eta][(1+v)^2 - 2]}{\dfrac{K_E K_F (1+v)^2}{[(1+v)^2(K_E - 4K_F) + 8K_F]} - \sqrt{2}c^2 I_B} = 0. \tag{21}$$

Defining the potential function

$$V(v) = \frac{[(K_S - 2c^2M_B)v^2 + \gamma v + \eta][(1+v)^2 - 2]}{\dfrac{K_E K_F (1+v)^2}{[(1+v)^2(K_E - 4K_F) + 8K_F]} - \sqrt{2}c^2 I_B}, \tag{22}$$

equation (21) can be rewritten in compact form as

$$\left(\frac{\mathrm{d}v}{\mathrm{d}\xi}\right)^2 + V(v) = 0 \tag{23}$$

and expresses the total energy conservation law for the Hamiltonian system

$$\begin{cases} \dfrac{\mathrm{d}v}{\mathrm{d}\xi} = y, \\ \dfrac{\mathrm{d}y}{\mathrm{d}\xi} = \dfrac{\mathrm{d}V}{\mathrm{d}v}, \end{cases} \tag{24}$$

where the quantity that is conserved is always equal to zero. This condition is equivalent to prescribing specific initial velocities

$$\left.\frac{\mathrm{d}v}{\mathrm{d}\xi}\right|_{\xi=0} \quad \text{and} \quad \left.\frac{\mathrm{d}y}{\mathrm{d}\xi}\right|_{\xi=0}. \tag{25}$$

The solutions of the Hamiltonian system described above correspond to periodic oscillations about the local minima of the potential V. In particular, they consist of periodic sequences of monotonic parts $v(\xi)$, whose inverses are given by

$$\xi(v) = \xi_0 \pm \int_{v(\xi_0)}^{v} \frac{1}{\sqrt{-V(\bar{v})}}\,\mathrm{d}\bar{v}. \tag{26}$$

At this stage, the objective is to determine whether the waveguide supports the propagation of axial displacement shock waves, that is, whether a (regularized) shock-type solution $\tilde{u}(\xi)$ exists, characterized by a nonperiodic profile with a distinct front, such that its derivative with respect to the phase variable ξ yields a solitary waveform. Observing that

$$v := \frac{\mathrm{d}\tilde{u}}{\mathrm{d}\xi} = \frac{\mathrm{d}\tilde{u}}{\mathrm{d}s} \tag{27}$$

when the function $\tilde{u}(\xi)$ is a waveform of shock type, the function $v(\xi)$ is then to be referred to as *axial strain solitary wave*. For $\xi \to \pm\infty$, for a solution $\tilde{u}(\xi)$ to be a shock waveform, the following conditions must be met:

$$v \to 0 \quad \text{and} \quad \frac{\mathrm{d}v}{\mathrm{d}\xi} \to 0. \tag{28}$$

The second condition ensures that $v \to 0$ as $\xi \to \pm\infty$, without inducing high-frequency oscillations. Taking the limit $\xi \to \pm\infty$ in (23), these conditions imply $V(0) = 0$. Imposing this requirement on the

expression of V in (22) yields that axial displacement shock wave propagation is only possible if $\eta = 0$. Furthermore, a Weierstrass-type qualitative analysis of the dynamical system (24) indicates that, for the function $v(\xi)$ to describe a symmetric solitary wave, the point $v = 0$ must correspond to a local maximum of $V(v)$, and the potential must admit a zero in the interval $[-1, \sqrt{2}-1]$, including the endpoints. To ensure that $v = 0$ is a local maximum, one first imposes the condition

$$\frac{\mathrm{d}V}{\mathrm{d}v}(0) = -\frac{\gamma}{\frac{K_E K_F}{K_E+4K_F} - \sqrt{2}c^2 I_B} = 0, \tag{29}$$

which leads to the conclusion that the constant γ should vanish, too. Therefore, up to now, the existence conditions for a displacement wave of shock type have led to the following form for the potential associated to the Hamiltonian dynamical system (24):

$$V(v) = \frac{(K_S - 2c^2 M_B)v^2[(1+v)^2 - 2]}{\frac{K_E K_F (1+v)^2}{[(1+v)^2(K_E-4K_F)+8K_F]} - \sqrt{2}c^2 I_B}. \tag{30}$$

Restrictions on the material parameters K_S, K_E, K_F, M_B, and I_B, all greater than or equal to zero, and wave velocity c shall now be sought so as to meet the condition

$$\frac{\mathrm{d}^2 V}{\mathrm{d}v^2}(0) < 0.$$

Elementary computations lead to

$$\frac{\mathrm{d}^2 V}{\mathrm{d}v^2}(0) = -\frac{2(K_S - 2c^2 M_B)}{\frac{K_E K_F}{K_E+4K_F} - \sqrt{2}c^2 I_B} < 0. \tag{31}$$

It is worth noting that, for any set of material parameters and wave velocity satisfying the above inequality, the potential function V admits exactly two zeros within the interval $0 \le 1 + v \le \sqrt{2}$, namely $v = 0$ and $v = \sqrt{2} - 1$. This implies that the considered monolayered pantographic waveguides support the propagation of axial strain solitary waves, and that only rarefaction-type solitary waves, rather than compressive ones, are admissible. Note also that, since the analyzed system is reciprocal, if the inequality above is satisfied by $c = c_0$ then it is satisfied also by $c = -c_0$. Furthermore, as $K_E \to \infty$, which means that the bar rigidity hypothesis holds, the inequality above becomes

$$\frac{K_S - 2c^2 M_B}{K_F - \sqrt{2}c^2 I_B} > 0.$$

	K_S	M_B	K_F	I_B	K_E	c^2
first dataset	10 20 30	10 20 30	0.5 1 1.5	0.5 1 1.5		
second dataset	20	20	1	1	10 10^2 10^3	0.25

Table 1. Numerical values considered for the stiffness and inertial parameters and the wave velocity at the continuum scale.

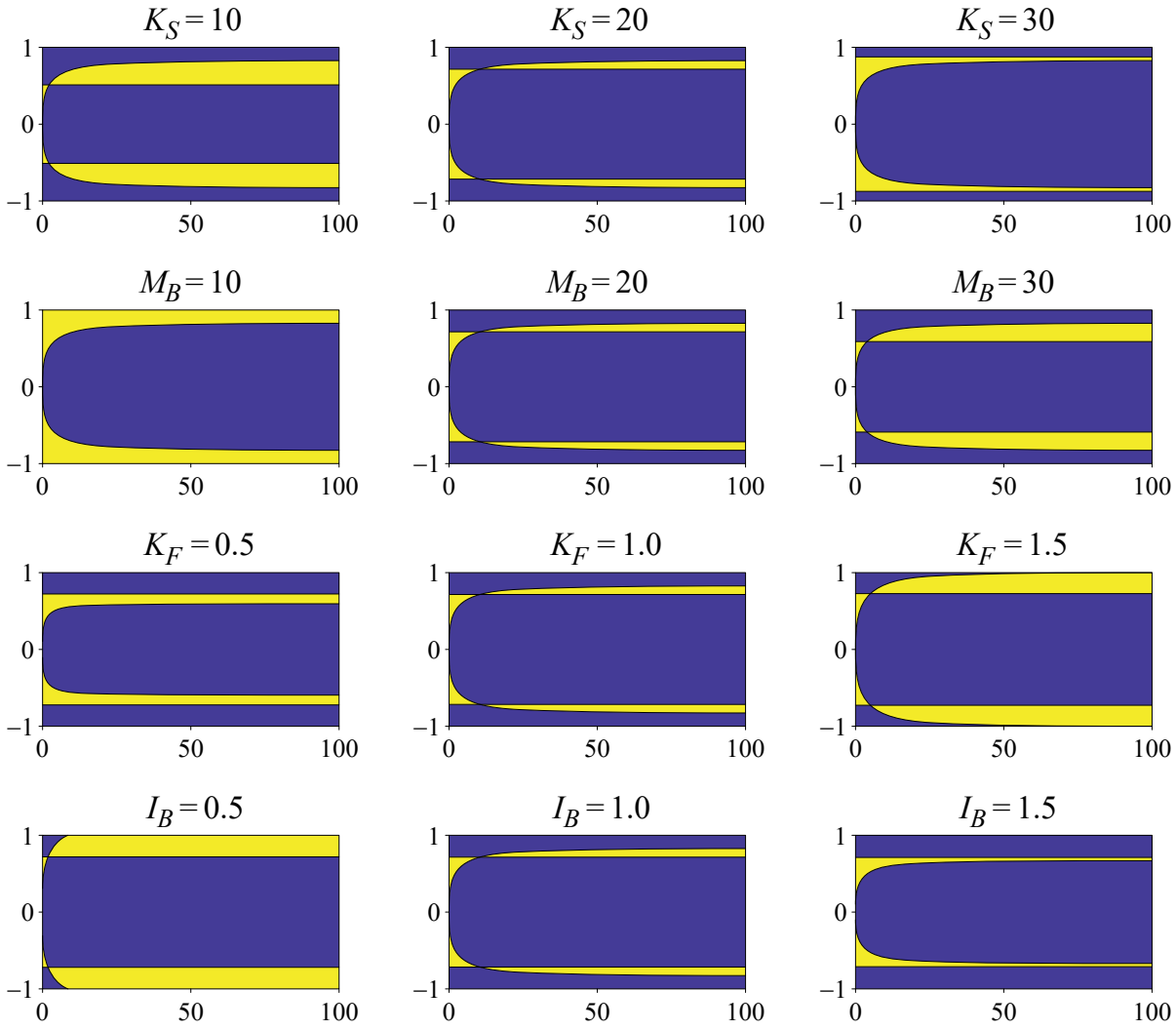

Figure 2. Regions of solitary wave propagation admissibility in the $K_E - c$ plane for the values of the material parameters (stiffness and inertial) in the first dataset of Table 1. Admissible regions are colored in blue.

Figure 2 shows the regions of solitary wave propagation admissibility in the $K_E - c$ plane when the parameters K_S, M_B, K_F, and I_B are varied according to the first dataset of Table 1. Admissible regions are colored in blue. For brevity, units of measure have been omitted: all numerical values are understood to be in the international system of units, here and throughout the paper.

4. Solitary waveforms

This section deals with the computation of solitary waveforms for several values of the parameter $K_E > 0$, while all other parameters are fixed, according to the second dataset in Table 1. The computation of the solitary waveform v has been performed by computing numerically, at first, the functions $\xi^-(v)$

and $\xi^+(v)$, with $v \in (0, \sqrt{2}-1]$, by means of (26),

$$\xi^{\mp}(v) = \pm \int_{\sqrt{2}-1}^{v} \frac{1}{\sqrt{-\dfrac{(K_S - 2c^2 M_B)\bar{v}^2[(1+\bar{v})^2-2]}{\dfrac{K_E K_F (1+\bar{v})^2}{[(1+\bar{v})^2(K_E-4K_F)+8K_F]} - \sqrt{2}c^2 I_B}}} \, \mathrm{d}\bar{v}, \tag{32}$$

where $\xi_0 = 0$ has been chosen arbitrarily. The functions $\xi^-(v)$ and $\xi^+(v)$ are monotonic and, once computed, can be inverted to obtain $v(\xi^-)$ and $v(\xi^+)$. The full solitary waveform is then reconstructed by symmetrically joining these two branches. Notably, for $v \in (0, \sqrt{2}-1]$, the integral in (32) always yields finite values, attaining zero at $v = \sqrt{2}-1$, while becoming improper, and in fact divergent, at $v = 0$. This divergence follows from the fact that $v = 0$ is a stationary point of $V(v)$, combined with the uniqueness of solutions to the Hamiltonian system (24). The derivative of the displacement waveform $\tilde{u}(\xi)$ with respect to ξ, i.e., the axial strain or stretch waveform $v(\xi)$, exhibits a bell-shaped profile with a single crest reaching $\sqrt{2}-1$. At the microscale, this corresponds to the square cell at the wavefront collapsing into a horizontal segment. Due to the construction method, the stretch solitary waveform $v(\xi)$ is even (symmetric about $\xi = 0$) and possesses a single peak.

Figure 3 presents the results of a numerical study conducted according to the procedure outlined above, for various values of the parameter K_E, i.e., $K_E = 10,\ 100,\ 1000$. In this study, the displacement waveform $\tilde{u}$ was obtained by integrating the function v, under the assumption that $\tilde{u} \to 0$ as $\xi \to -\infty$. Owing to the singular behavior of the integrand in (32), the computation of $v(\xi)$ was carried out using the NIntegrate function of the commercial software Mathematica with default settings. Subsequently, $\tilde{u}(\xi)$ was computed via numerical integration using the cumtrapz command in MATLAB. The phase variable ξ was defined over the interval $[-20, 20]$ — sufficiently wider than the effective support of the solitary waveform — and discretized using 1000 points for integration.

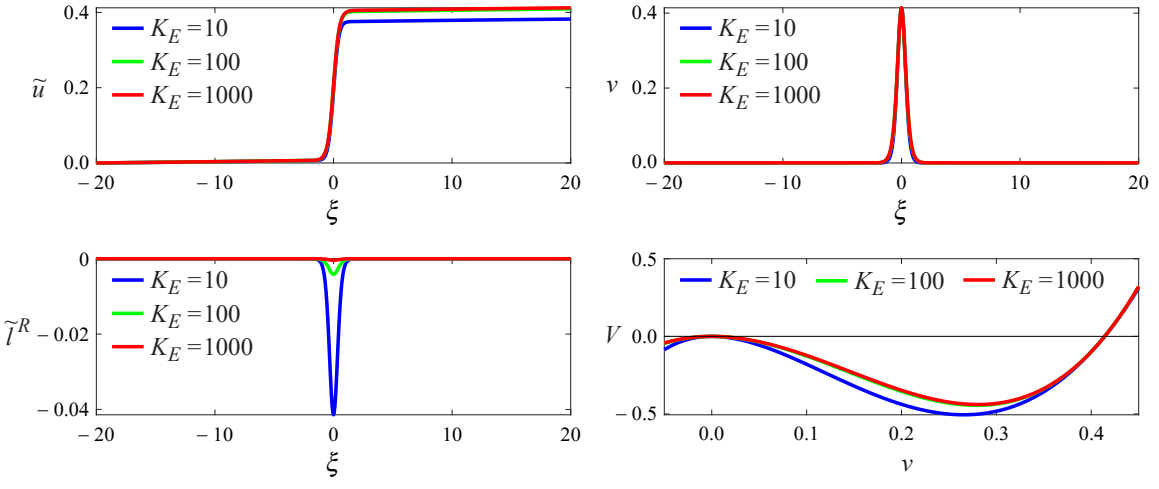

Figure 3. Displacement $\tilde{u}$ (top left), stretch v (top right) and microstretch $\tilde{l}^R$ (bottom left) waveforms against the phase variable ξ, for various values of K_E. Bottom right: potential function $V(v)$, for various values of K_E.

5. Time-dependent microscale simulations

This section presents time-dependent simulations of the discrete micromodel, aimed at verifying the solitary wave propagation predicted by the continuum theory. To solve the discrete system directly, without relying on the assumptions made in the derivation of the continuum model, it is advantageous to introduce an alternative global, minimal set of generalized coordinates, distinct from the one employed in the homogenization process: the kinematics of the discrete system is entirely described by the displacements q_i of the nodal points. Unlike the micromodel employed in the homogenization, all nodes of the microstructure were endowed with a mass m, while links were considered massless. Nevertheless, it is easy to prove that this choice yields a system equivalent to the one employed in the homogenization [72]. The Euler–Lagrange equations

$$\frac{\partial \mathcal{U}_\varepsilon}{\partial q_i} + m\ddot{q}_i = 0 \tag{33}$$

were reduced to an initial value problem with initial data on q_i and $\dot{q}_i$ and were solved through the command $ode23t$ of the commercial software Matlab. A series of parametric analyses was conducted, each varying a single stiffness, inertial, loading, or geometric parameter, for both single- and double-tug test configurations. All displacement variables were initialized to zero, and out-of-plane displacements of central nodes were constrained to vanish. Each unit cell was assigned a unit length; Figure 4 illustrates the node numbering scheme for a representative monolayered pantographic waveguide composed of 20 cells.

In the single-tug test, the leftmost central node (node 3 in Figure 4) is fixed, while a horizontal displacement of the form

$$\frac{u_{\max}}{1+\exp(-h(t-t_0))} \tag{34}$$

is applied to the rightmost central node (node 60 in Figure 4), where $u_{\max},\ h,\ t_0 > 0$ denote the maximum displacement, the steepness of the transition, and the time at which half the maximum displacement is applied, respectively. It is worth noting that when the shear stiffness k_S is set to zero, the single-tug test would, in a quasistatic regime, enable the system to exploit the zero-energy deformation mode described in (4), thereby minimizing the deformation energy subject to the imposed kinematic constraints. However, inertial effects inhibit this mechanism, and the prescribed boundary conditions in the dynamic setting are sufficient to suppress the activation of the floppy mode. Figure 5 displays the time evolution of the applied displacement (top) and its time derivative (bottom), normalized by setting $u_{\max} = 1$ for the case $h = 15,\ t_0 = 1$.

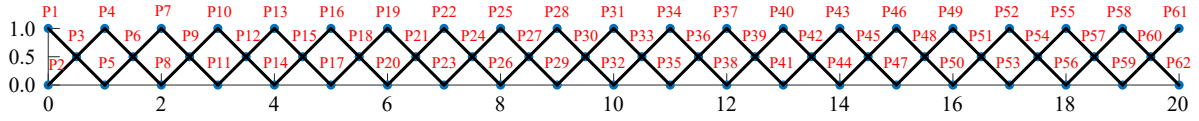

Figure 4. Node numbering in a monolayered pantographic waveguide with 20 cells.

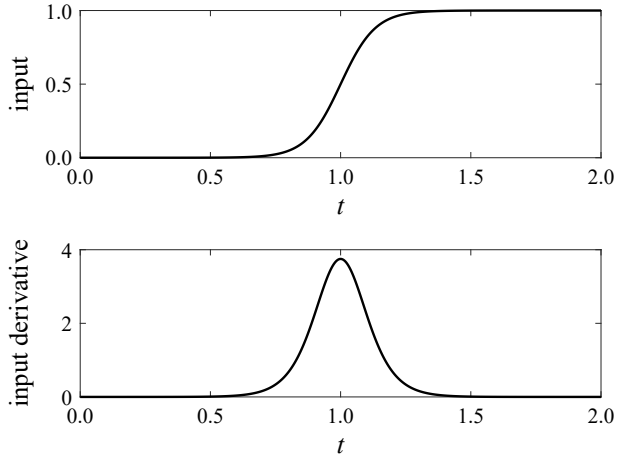

Figure 5. The applied displacement (top) and its time derivative (bottom) against time for $h = 15$ and $t_0 = 1$.

k_S	m	k_F	k_E		h		# cells			$u_{\max}$	t_0
10	8	10	10	10^5	15	40	20	40	41	0.8	1

Table 2. Numerical values considered for the stiffness, inertial, and load parameters for time-dependent simulations at the discrete microscale.

Table 2 lists the numerical values assigned to stiffness, inertial, loading, and geometrical parameters used in the time-dependent simulations of the discrete micromodel.

For reference, a single-tug test is first presented with parameters $k_E = 10^5$ (corresponding to quasi-inextensible oblique bars), $h = 40$, and $N = 40$. Figure 6 illustrates the deformed configurations of the monolayered pantographic waveguide at various time instants. Figure 7 shows the time evolution of the energy contributions (left, E_{ext} and $E_{\text{ext}}^{\text{bis}}$ denote the energy stored in the oblique bars and extensional springs, respectively; other symbols are self-explanatory), the phase portrait (center), and the equilibrium path (right). The quantities $\|\boldsymbol{u}\|$ and $\|\boldsymbol{v}\|$ are obtained by computing the Euclidean norm of the vectors collecting all the q_i's and $\dot{q}_i$'s, respectively. The quantity $\|\boldsymbol{S}\|$ is obtained by computing the Euclidean norm of the vector collecting all the derivatives $\frac{\partial \mathcal{U}_\varepsilon}{\partial q_i}$. Figure 8 reports, at selected time instants, the axial displacement u of the central nodes (top left), the stretch Δu of the centerline (top right), and the absolute elongation of the left (bottom left) and right (bottom right) bars along the rectilinear abscissa. Finally, Figure 9 presents contour plots in the space-time plane of the axial displacement (left) and the stretch of the centerline (right).

The figures indicate that both the rate of applied displacement, controlled by the parameter h, and the maximum displacement amplitude are appropriate for inducing solitary wave propagation in the waveguide. Notably, the solitary wavefront consists of a single crest corresponding to the complete closure of a square cell, and the waveform exhibits the expected symmetric profile, in agreement with predictions from the continuum model. Figure 9 (right) confirms that the wave propagates at a constant velocity,

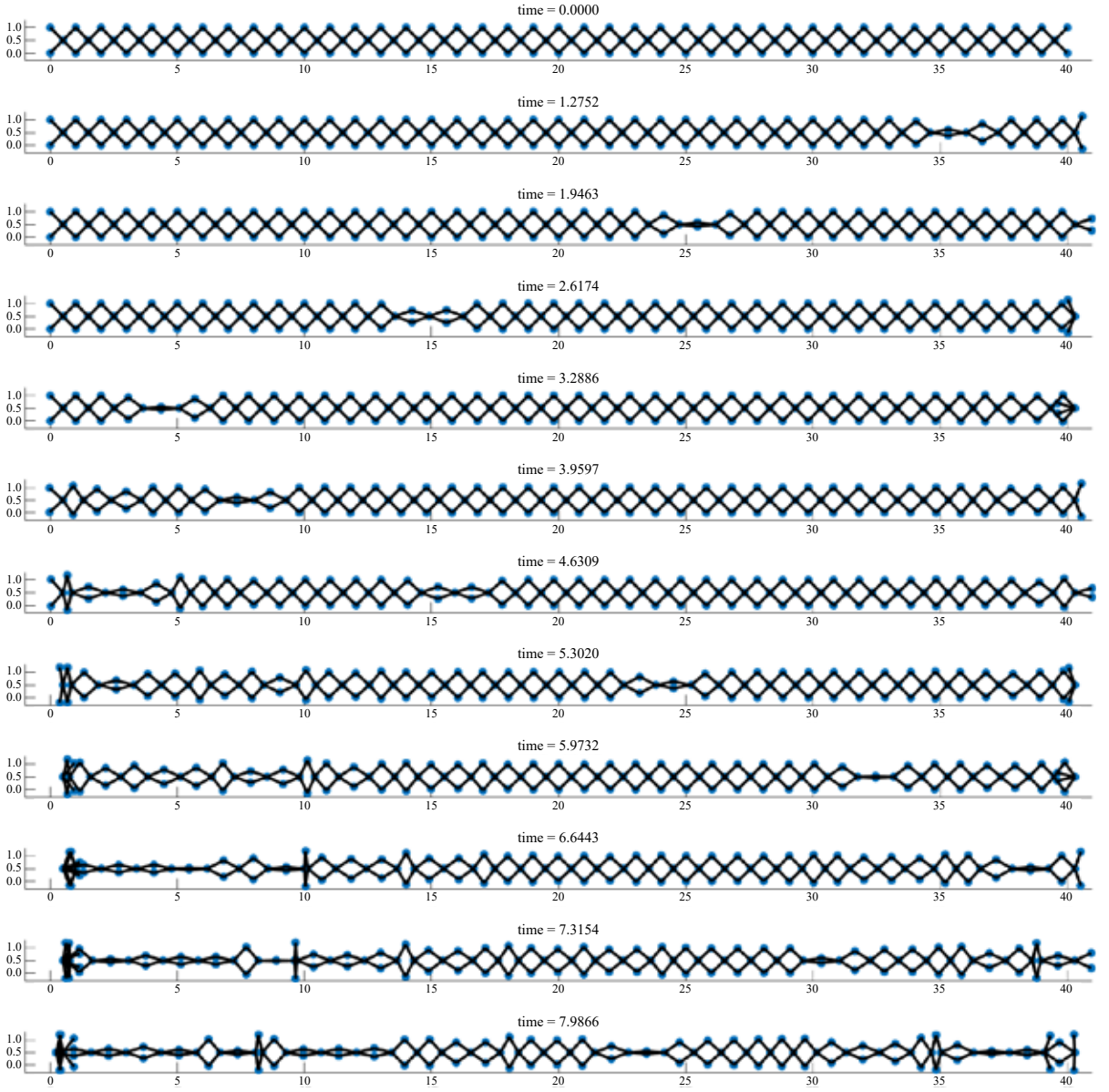

Figure 6. Deformed shapes of the monolayered pantographic waveguide with 40 cells at different time instants for a single-tug test with $k_E = 10^5$ and $h = 40$.

measured to be approximately $9/0.53512 \approx 16.81866$. Following the first full reflection, the solitary wave remains largely intact, though it travels at a slightly reduced constant speed and develops a trailing tail. After the second reflection, the wave further decelerates, and an additional tail emerges. Eventually, this tail interferes with the one generated by the first reflection, traveling in the opposite direction, leading the system toward thermalization. It is also worth noting that the four free bars located at the ends of the waveguide rotate with appreciable angular velocity. However, comparative simulations conducted without

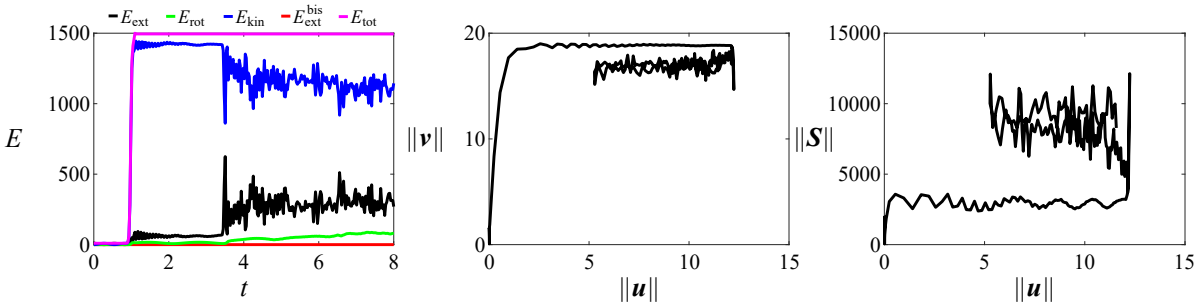

Figure 7. Contributions to the total energy against time (left), phase portrait (center), and equilibrium path (right) for the monolayered pantographic waveguide with 40 cells subjected to a single-tug test with $k_E = 10^5$ and $h = 40$.

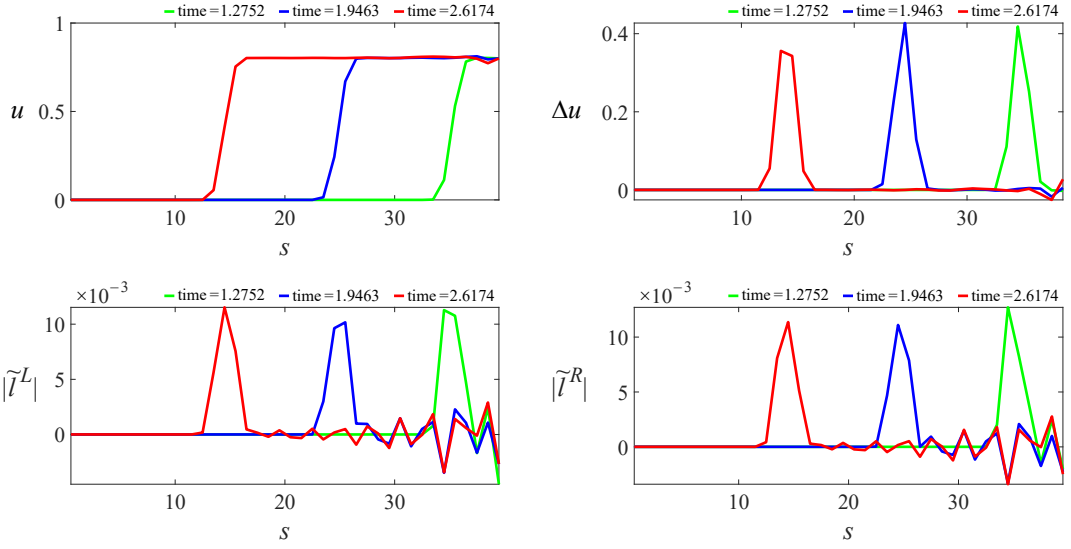

Figure 8. Axial displacement of the central points (top left), stretch of the centerline (top right), and absolute value of the elongation of the left (bottom left) and right (bottom right) bars against the rectilinear abscissa at different time instants for the monolayered pantographic waveguide with 40 cells subjected to a single-tug test with $k_E = 10^5$ and $h = 40$.

these bars, omitted here for brevity, suggest that their influence on solitary wave propagation is negligible. This effect is expected to vanish entirely in the limit as the number of cells tends to infinity. Most of the mechanical energy is of kinetic type.

The potential, deformation energy is mostly due to the deformation of the oblique bars. Deformation energy due to deformation of the extensional springs colored in blue in Figure 1 (top) is negligible. After the first reflection, due to the formation of a tail of the main wavefront, there is a significant quota of the kinetic energy that transforms into deformation energy, both stored in the deformation of the oblique bars and in the deformation of the rotational springs. This phenomenon does not occur after the second reflection, as the system is already close to complete thermalization by that point. However, a gradual

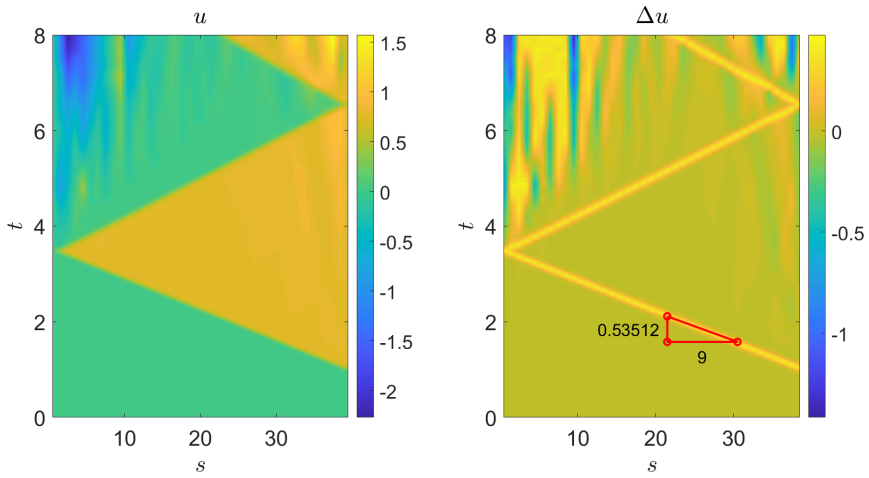

Figure 9. Contour plot of the axial displacement of the central points (left) and of the stretch of the centerline (right) in the space-time plane for the monolayered pantographic waveguide with 40 cells subjected to a single-tug test with $k_E = 10^5$ and $h = 40$.

equalization of kinetic and deformation energy is still observed. What has been described in the last four periods is observed in all numerical tests unless otherwise stated.

5.1. ***Sensitivity to the total cell number.*** In this subsection, the results of a single-tug test on a monolayered pantographic waveguide with 20 cells and $k_E = 10^5$ and $h = 40$ are reported.

Figure 10 shows the deformed shapes of the waveguide at different time instants. Figure 11 shows the contributions to the total energy against time (left), phase portrait (center), and equilibrium path (right). Figure 12 shows the axial displacement of the central points (top left), stretch of the centerline (top right), and absolute value of the elongation of the left (bottom left) and right (bottom right) bars against the rectilinear abscissa at different time instants. Figure 13 shows the contour plot of the axial displacement of the central points (left) and of the stretch of the centerline (right) in the space-time plane.

The results confirm that solitary wave propagation still occurs, exhibiting the same qualitative characteristics observed in the 40-cell case discussed in the previous subsection. In particular, the wavefront maintains a symmetric, localized structure with a single crest. The measured wave velocity in this test is $8/0.53512 \approx 14.94992$, which closely matches the velocity observed in the 40-cell configuration under identical stiffness, inertial, and loading parameters. This consistency aligns with the theoretical expectation that, as the number of cells increases, the wave velocity converges to a finite limit.

5.2. ***Sensitivity to the applied displacement rate.*** This subsection reports the results of a single-tug test on a monolayered pantographic waveguide composed of 40 cells, with $k_E = 10^5$ and $h = 15$.

The deformed shapes of the waveguide at selected time instants are shown in Figure 14. The evolution of the system's total energy (left), phase portrait (center), and equilibrium path (right) are presented in Figure 15. The axial displacement of the central points (top left), centerline stretch (top right), and the

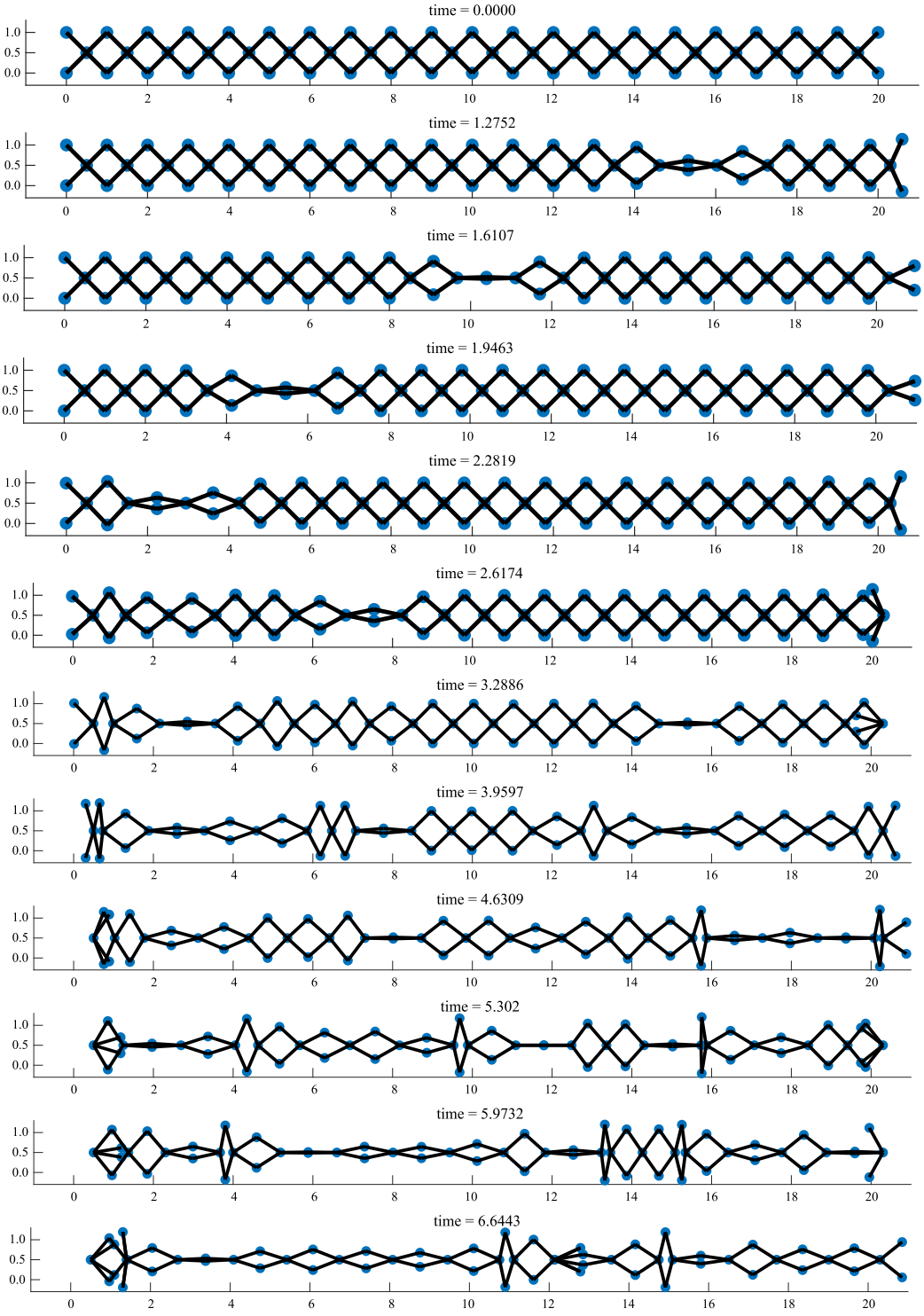

Figure 10. Deformed shapes of the monolayered pantographic waveguide with 20 cells at different time instants for a single-tug test with $k_E = 10^5$ and $h = 40$.

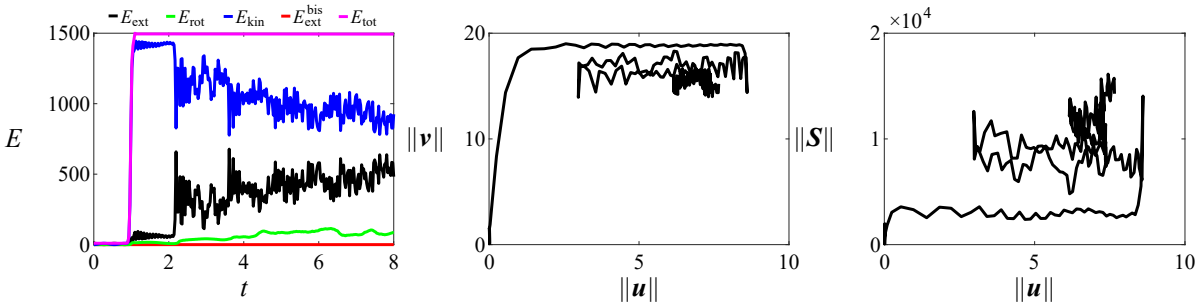

Figure 11. Contributions to the total energy against time (left), phase portrait (center), and equilibrium path (right) for the monolayered pantographic waveguide with 20 cells subjected to a single-tug test with $k_E = 10^5$ and $h = 40$.

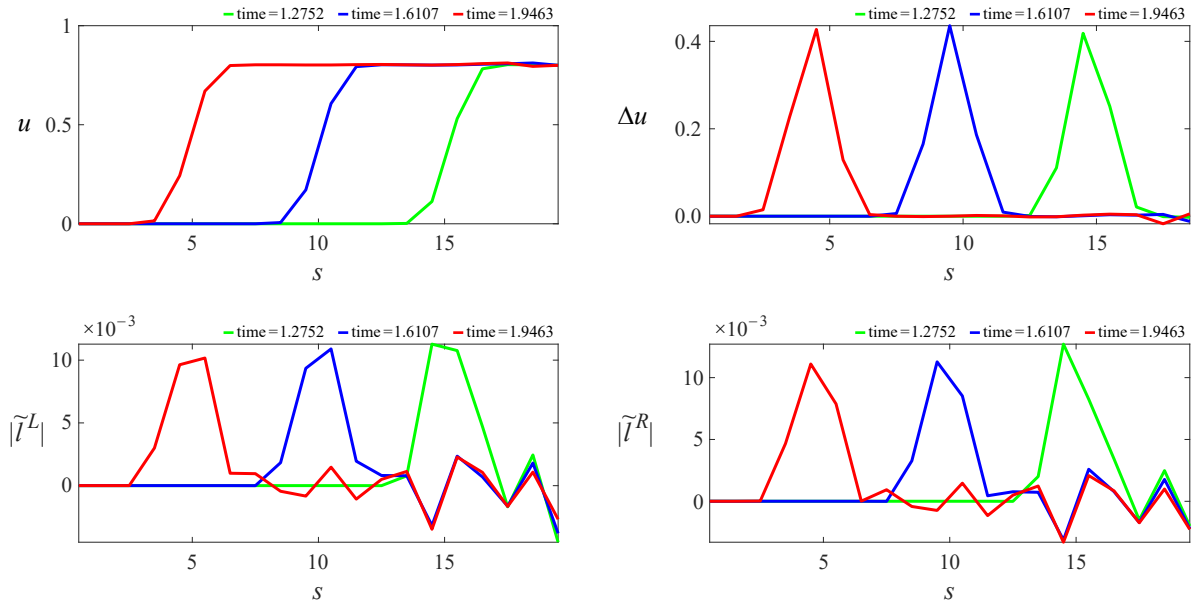

Figure 12. Axial displacement of the central points (top left), stretch of the centerline (top right), and absolute value of the elongation of the left (bottom left) and right (bottom right) bars against the rectilinear abscissa at different time instants for the monolayered pantographic waveguide with 20 cells subjected to a single-tug test with $k_E = 10^5$ and $h = 40$.

absolute elongation of the left (bottom left) and right (bottom right) bars versus the rectilinear abscissa at different times are shown in Figure 16. Finally, Figure 17 shows contour plots of the axial displacement (left) and the stretch of the centerline (right) in the space-time plane.

For the considered loading rate, a trailing tail forms at the onset of wave propagation and remains confined near the right end of the waveguide, traveling with a significantly lower velocity than the primary wavefront. Over time, the tail's amplitude gradually increases, while the amplitude of the main solitary wavefront slightly decreases. Unlike all the other tests presented in this paper, the potential, deformation energy is mostly due to the deformation of the rotational springs.

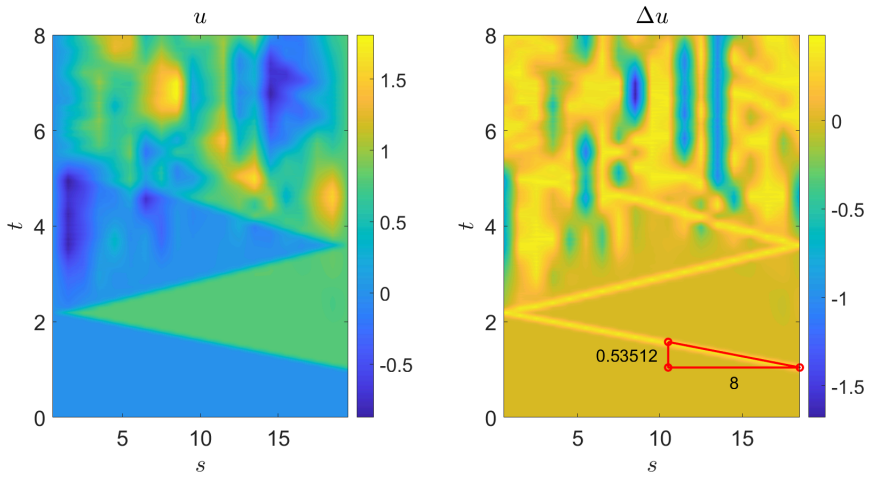

Figure 13. Contour plot of the axial displacement of the central points (left) and of the stretch of the centerline (right) in the space-time plane for the monolayered pantographic waveguide with 20 cells subjected to a single-tug test with $k_E = 10^5$ and $h = 40$.

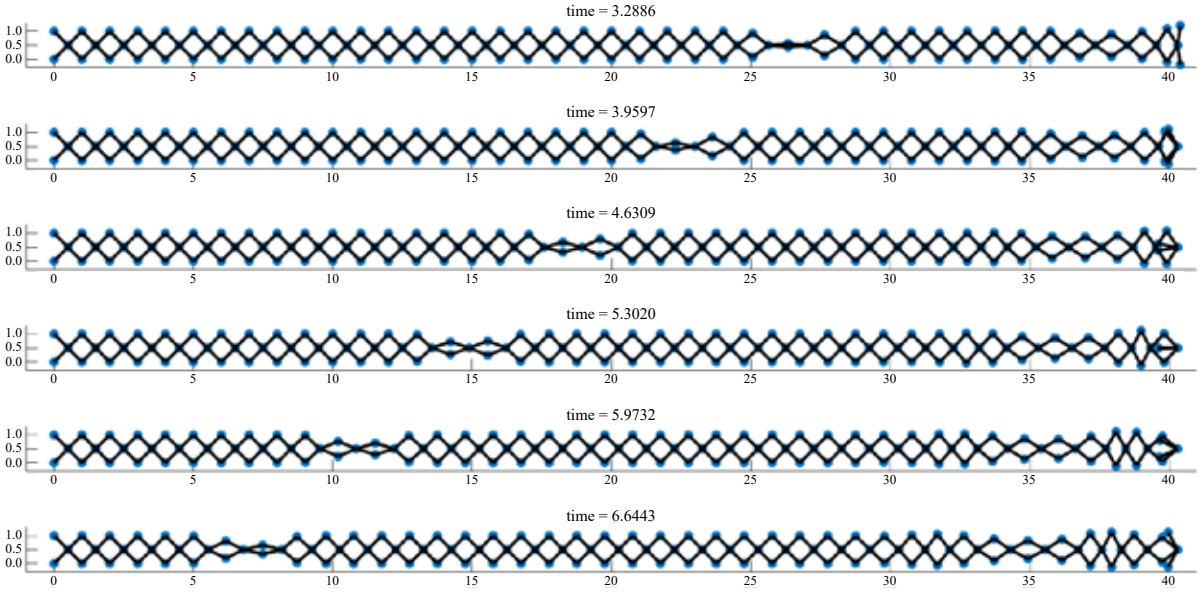

Figure 14. Deformed shapes of the monolayered pantographic waveguide with 40 cells at different time instants for a single-tug test with $k_E = 10^5$ and $h = 15$.

5.3. ***Sensitivity to the extensional stiffness.*** In this subsection, the results of a single-tug test on a monolayered pantographic waveguide with 40 cells and $k_E = 10$ and $h = 40$ are reported. Figure 18 shows the deformed shapes of the waveguide at different time instants. Other plots have been excluded due to their trivial nature. It can be concluded that, for the analyzed $k_E = 10$, the wave remains confined in proximity of the right end of the waveguide.

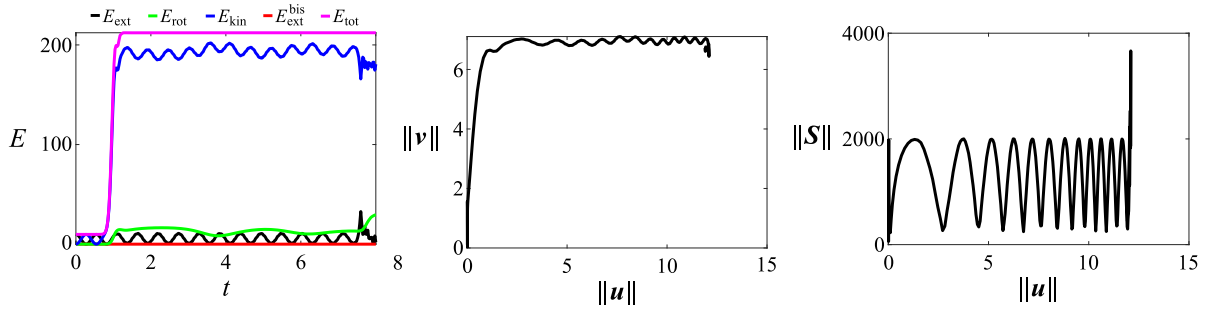

Figure 15. Contributions to the total energy against time (left), phase portrait (center), and equilibrium path (right) for the monolayered pantographic waveguide with 40 cells subjected to a single-tug test with $k_E = 10^5$ and $h = 15$.

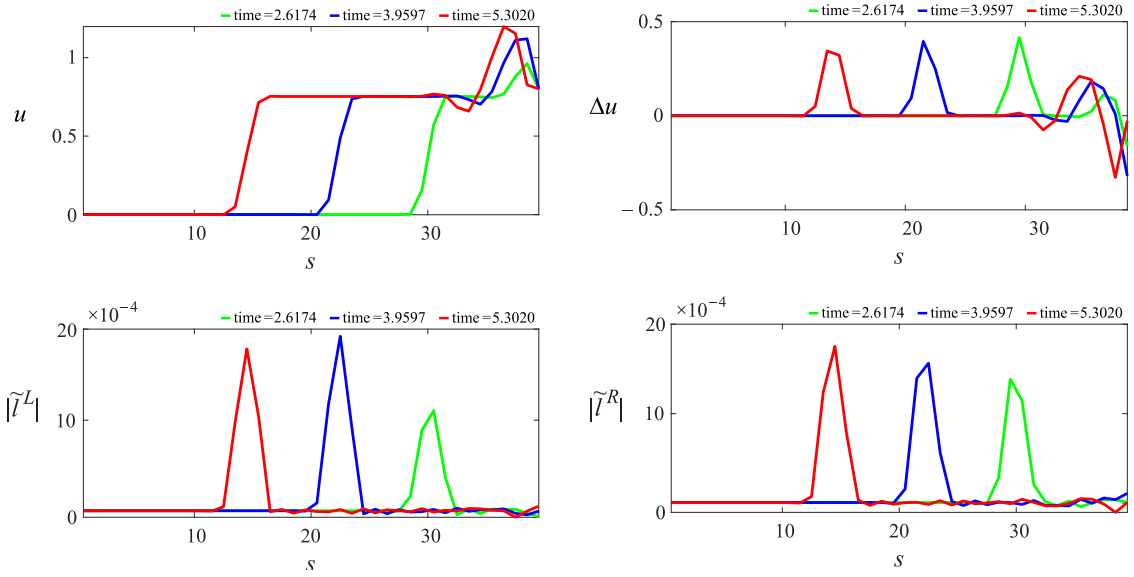

Figure 16. Axial displacement of the central points (top left), stretch of the centerline (top right), and absolute value of the elongation of the left (bottom left) and right (bottom right) bars against the rectilinear abscissa at different time instants for the monolayered pantographic waveguide with 40 cells subjected to a single-tug test with $k_E = 10^5$ and $h = 15$.

5.4. ***Collision of two solitary waves: odd number of cells.*** In this subsection, the results of a double-tug test on a monolayered pantographic waveguide with 41 cells and $k_E = 10^5$ and $h = 40$ are reported. In such a test, a displacement

$$\frac{u_{\max}}{1+\exp(-h(t-t_0))} \tag{35}$$

is applied to the rightmost central point, i.e., node 60 in Figure 4, and a displacement

$$-\frac{u_{\max}}{1+\exp(-h(t-t_0))} \tag{36}$$

is applied to the leftmost central point, i.e., node 3 in Figure 4.

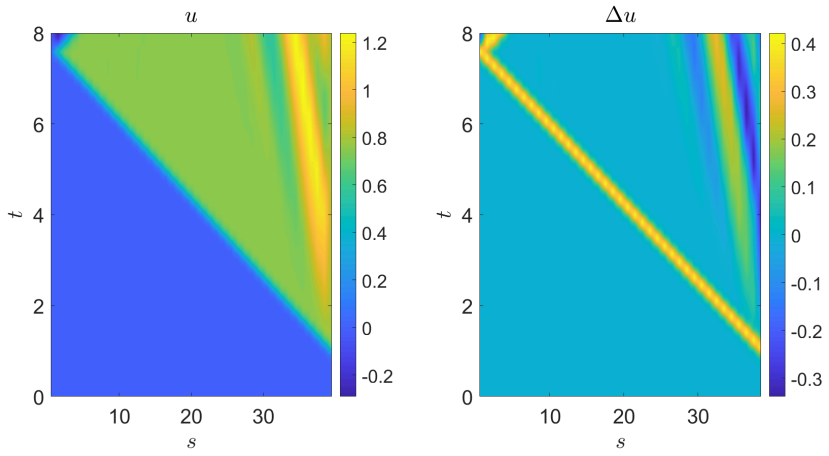

Figure 17. Contour plot of the axial displacement of the central points (left) and of the stretch of the centerline (right) in the space-time plane for the monolayered pantographic waveguide with 40 cells subjected to a single-tug test with $k_E = 10^5$ and $h = 15$.

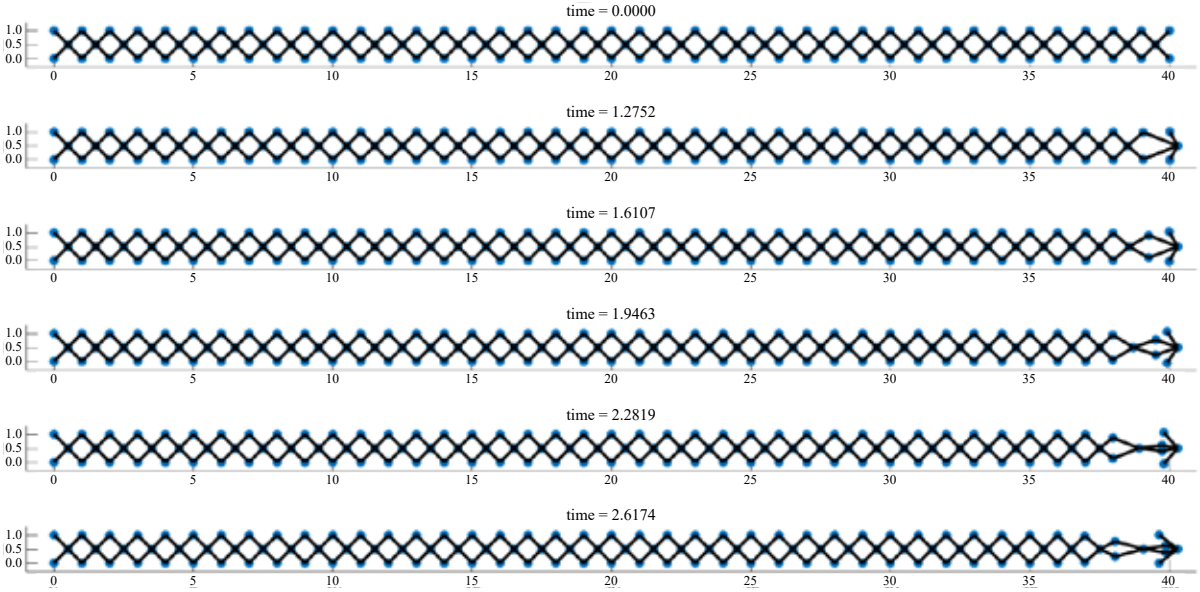

Figure 18. Deformed shapes of the monolayered pantographic waveguide with 20 cells at different time instants for a single-tug test with $k_E = 10^5$ and $h = 40$.

Figure 19 shows the deformed shapes of the waveguide at different time instants. Contributions to the total energy against time (left), phase portrait (center), and equilibrium path (right) are shown in Figure 20. Figure 21 shows the axial displacement of the central points (top left), stretch of the centerline (top right), and absolute value of the elongation of the left (bottom left) and right (bottom right) bars against the rectilinear abscissa at different time instants. Finally, Figure 22 shows the contour plot of the axial displacement of the central points (left) and of the stretch of the centerline (right) in the space-time plane.

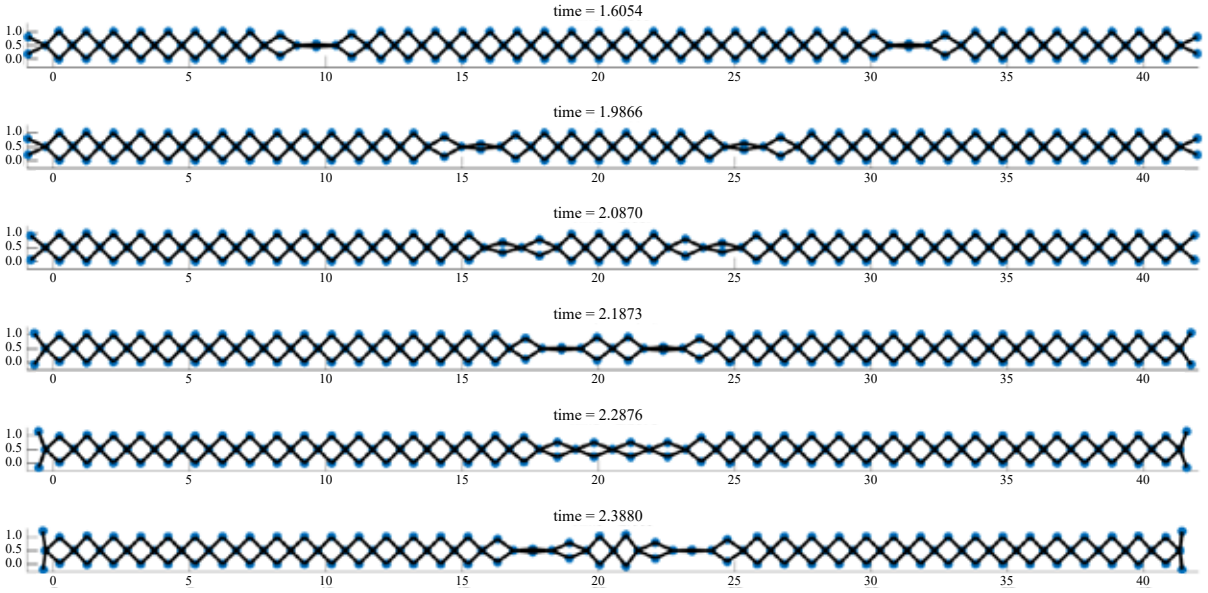

Figure 19. Deformed shapes of the monolayered pantographic waveguide with 41 cells at different time instants for a double-tug test with $k_E = 10^5$ and $h = 40$.

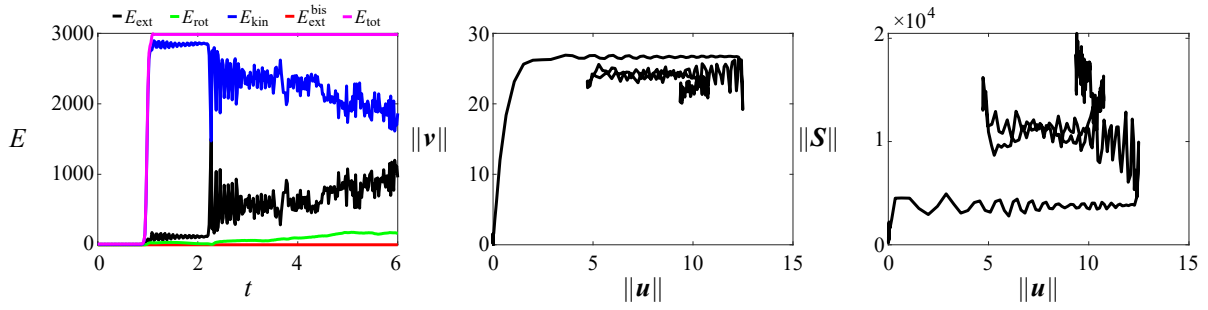

Figure 20. Contributions to the total energy against time (left), phase portrait (center), and equilibrium path (right) for the monolayered pantographic waveguide with 41 cells subjected to a double-tug test with $k_E = 10^5$ and $h = 40$.

It is observed that, after the collision, the two solitary waves emerge only partially unaltered. The wave resulting from the combination of the two solitary waves has a maximum amplitude slightly more than $\Delta u = \sqrt{2} - 1$ ($\Delta u = 0.4982$), which is due to the fact that when a square cell is completely closed, since the oblique bars are extremely stiff, Δu cannot increase significantly beyond the value $\sqrt{2} - 1$. After the collision, the two main wavefronts maintain the property $\Delta u \approx \sqrt{2} - 1$, while the fluctuations emerging in between them seem to have a moderate amplitude and propagate much slower than the main wavefronts. After the second reflection, although the energy is conserved, the systems perceptibly looses its symmetry in space, most likely due to a small numerical error that propagates in time.

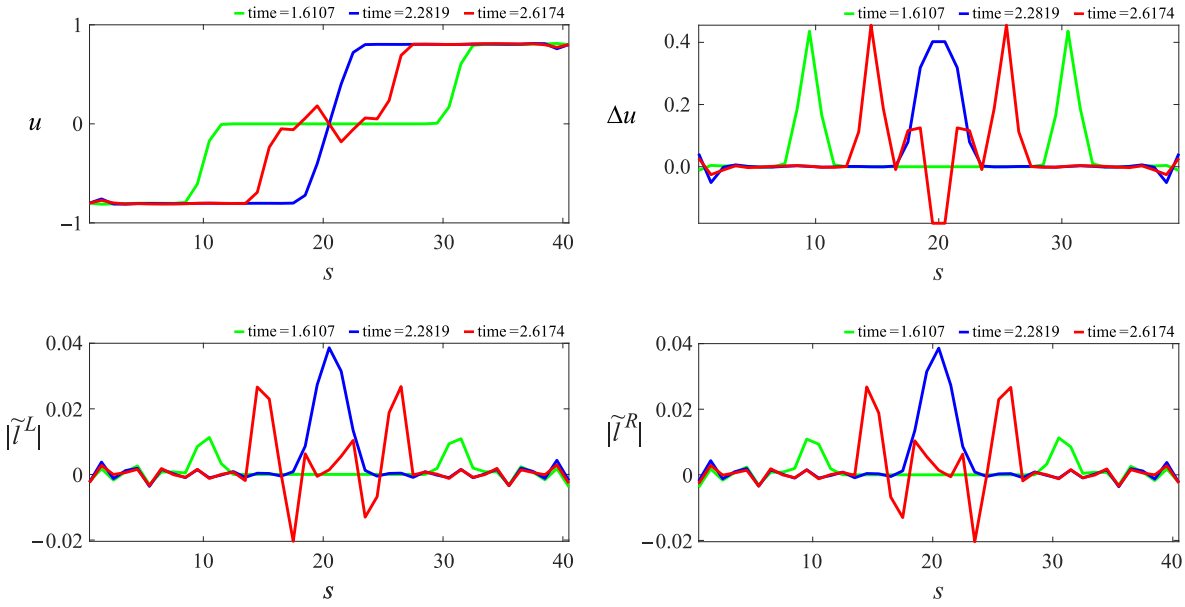

Figure 21. Axial displacement of the central points (top left), stretch of the centerline (top right), and absolute value of the elongation of the left (bottom left) and right (bottom right) bars against the rectilinear abscissa at different time instants for the monolayered pantographic waveguide with 41 cells subjected to a double-tug test with $k_E = 10^5$ and $h = 40$.

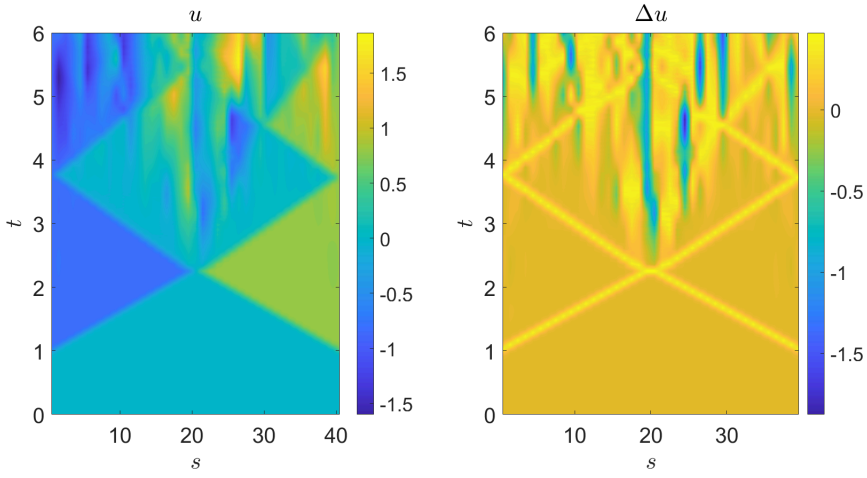

Figure 22. Contour plot of the axial displacement of the central points (left) and of the stretch of the centerline (right) in the space-time plane for the monolayered pantographic waveguide with 41 cells subjected to a double-tug test with $k_E = 10^5$ and $h = 40$.

5.5. ***Collision of two solitary waves: even number of cells.*** This subsection presents the results of a double-tug test conducted on a monolayered pantographic waveguide composed of 40 cross cells, with parameters $k_E = 10^5$ and $h = 40$.

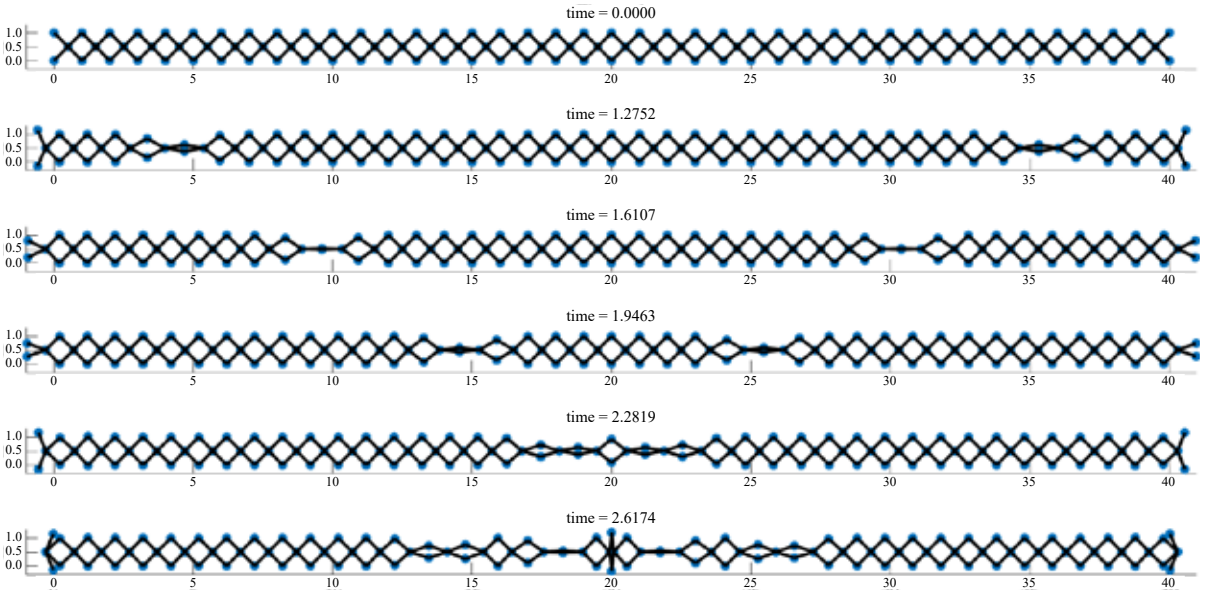

Figure 23. Deformed shapes of the monolayered pantographic waveguide with 40 cells at different time instants for a double-tug test with $k_E = 10^5$ and $h = 40$.

The deformed configurations at selected time instants are shown in Figure 23. The evolution of the total energy components over time (left), the phase portrait (center), and the equilibrium path (right) are illustrated in Figure 24. Figure 25 reports the axial displacement of the central nodes (top left), the centerline stretch (top right), and the absolute elongation of the left (bottom left) and right (bottom right) bars with respect to the rectilinear abscissa at different time instants. The contour plots in Figure 26 show the spatiotemporal distribution of axial displacement (left) and centerline stretch (right).

The results indicate that the solitary waves initiated at the two ends of the waveguide do not retain their original form after collision. The postcollision waveform reaches a maximum amplitude slightly exceeding $\Delta u = \sqrt{2} - 1$ ($\Delta u = 0.5267$). The occurrence $\Delta u = \sqrt{2} - 1$ corresponds to the complete collapse of a square cell and, due to the high axial stiffness of the oblique bars, further extension is limited. While the main wavefronts persist after the interaction with amplitudes close to $\Delta u \approx \sqrt{2} - 1$, the region between them becomes dominated by oscillatory components whose amplitudes surpass those of the primary fronts are characterized by two propagating tails with velocity slightly lower than that of the main wavefronts. A noteworthy behavior occurs at the center of the waveguide: the centrally located cell folds entirely into a vertical segment, resulting in $\Delta u \approx -1$, persistently in time. This phenomenon does not arise when the number of cross cells is odd, as no cell is positioned precisely at the midpoint to be directly affected by the symmetric collision. This observation highlights the influence of the cell count parity on the postcollision configuration. The overall dynamics bear resemblance to those observed in architected soft materials reported in [30], where networks of squares joined by deformable ligaments support elastic vector solitons. In that context, solitons undergoing corotational motion were observed to emerge unaltered from collisions, whereas counterrotating solitons displayed repulsive, nonpenetrative

interactions. It must be emphasized that the homogenized continuum model employed in this analysis does not encode the parity of the number of cells. As such, the continuum framework, in its current form, is inherently unable to capture postcollision asymmetries. Enriching the continuum model with suitable microstructural descriptors would be required to reproduce the observed behavior accurately. Also in this case, after the second reflection, although the energy is conserved, the systems perceptibly looses its symmetry in space, most likely due to a small numerical error that propagates in time.

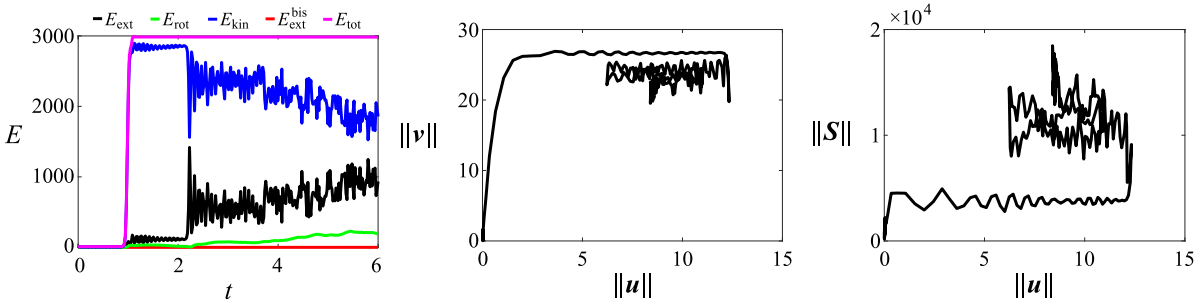

Figure 24. Contributions to the total energy against time (left), phase portrait (center), and equilibrium path (right) for the monolayered pantographic waveguide with 40 cells subjected to a double-tug test with $k_E = 10^5$ and $h = 40$.

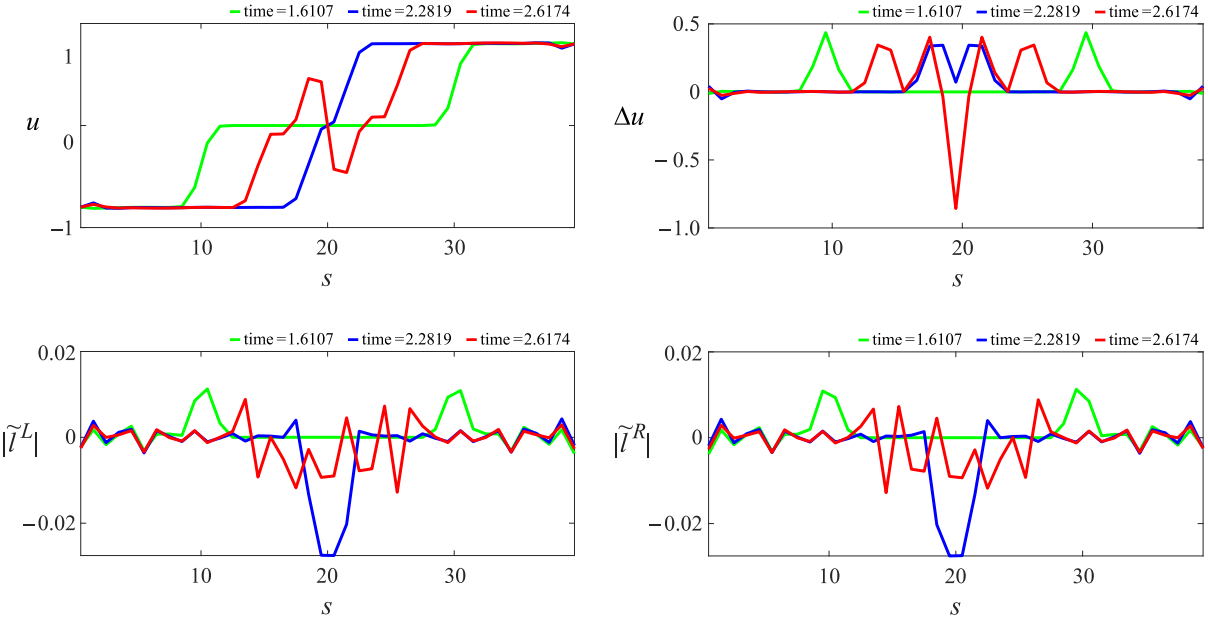

Figure 25. Axial displacement of the central points (top left), stretch of the centerline (top right), and absolute value of the elongation of the left (bottom left) and right (bottom right) bars against the rectilinear abscissa at different time instants for the monolayered pantographic waveguide with 40 cells subjected to a double-tug test with $k_E = 10^5$ and $h = 40$.

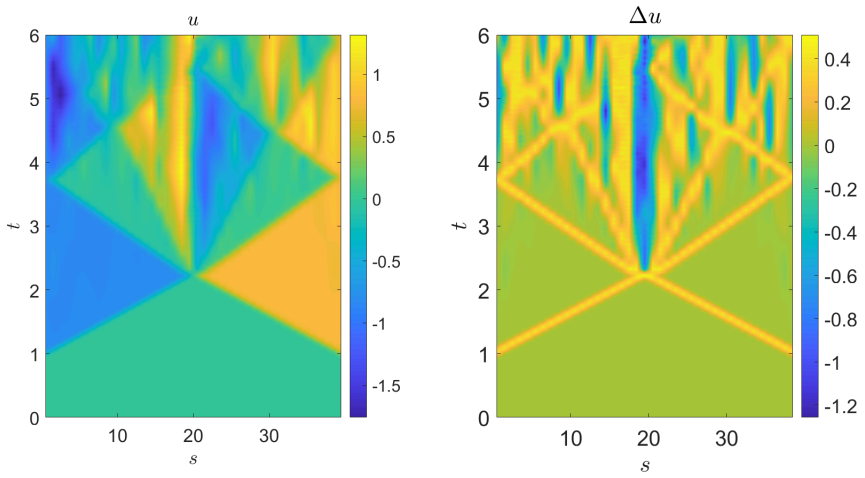

Figure 26. Contour plot of the axial displacement of the central points (left) and of the stretch of the centerline (right) in the space-time plane for the monolayered pantographic waveguide with 40 cells subjected to a double-tug test with $k_E = 10^5$ and $h = 40$.

6. Conclusions

This paper has investigated monolayered pantographic waveguides composed of nearly inextensible flexural elements, aiming to assess the hypothesis that elastic solitary waves can propagate through such structures. A homogenized continuum model, based on Hookean interaction potentials at the microscale, has been developed. By introducing a traveling wave ansatz into the continuum Lagrangian, the problem has been reformulated as that of a particle moving along a curve under a potential, with the phase variable serving as time.

A qualitative Weierstrass analysis of the potential has revealed that the system admits rarefaction-type elastic solitary waves, specifically of the stretch type. Inequalities on the material parameters ensuring the existence of solitary waves with a prescribed velocity have been derived. These solitary waves have been shown to be symmetric, featuring a single crest, consistent with the behavior identified in [5] for certain nonlinear, nonlocal dispersive equations, including the Whitham and Whitham–Boussinesq systems.

To validate the continuum model and explore key parametric effects, detailed time-dependent simulations of the discrete system have been performed. In particular, the influence of the number of cells, loading rate, and flexural elements' extensional stiffness on solitary wave propagation has been examined. Wave interaction dynamics has also been analyzed: for an odd number of cells, solitary waves emerge from collisions largely unaltered, whereas for an even number of cells, extreme compression occurs between the wave crests, leading to full cell closure and the formation of two propagating tails. It is worth mentioning that in Figures 9, 13, 22, and 26, at certain time-space locations, that the relative displacement between adjacent central cells is less than -1, which implies that two material points along the centerline mutually penetrate. Indeed, the individual cells have a unit longitudinal length. While this violates the continuum model's assumptions, which excludes such mutual penetration, it does not reflect numerical

issues. It rather reflects a meaningful physical phenomenon beyond the scope of the current assumptions or a modeling artifact, depending on the actual realization of the studied pantographic waveguides.

Future research directions include extending the study to monolayered pantographic waveguides incorporating dissipative effects [39; 45; 74] and investigating solitary wave propagation in multilayered pantographic waveguides by combining the reduced one-dimensional model from [17] with the approach developed herein. Further interesting researches could also aim at validating the present findings leveraging swarm-based models [22; 23; 24; 25], as well as conducting experimental studies [67].

Appendix

In this appendix, the least action principle, considering kinematically admissible variations δu depending on the variable ξ, is analyzed. Admissible variations $\delta u(s,t) = \delta\tilde{u}(s-ct)$ are a subclass of those to be considered to ensure the stationarity of the action functional corresponding to the Lagrangian (16) for a wave solution $\tilde{u}(s-ct)$. Therefore, their use to derive Euler–Lagrange equations is intended to provide only a necessary condition for $\tilde{u}(s-ct)$ to be a stationary point of the action functional. That said, considering $\delta u(s,t) = \delta\tilde{u}(s-ct)$, leads to the Euler–Lagrange equation

$$\frac{\mathrm{d}^2}{\mathrm{d}\xi^2}\left(\frac{\partial\mathscr{L}}{\partial\left(\frac{\mathrm{d}^2\tilde{u}}{\mathrm{d}\xi^2}\right)}\right) - \frac{\mathrm{d}}{\mathrm{d}\xi}\left(\frac{\partial\mathscr{L}}{\partial\left(\frac{\mathrm{d}\tilde{u}}{\mathrm{d}\xi}\right)}\right) = 0, \tag{37}$$

where $\mathscr{L}$ is the Lagrangean density. Equation (37) can be integrated once leading to the condition

$$\frac{\mathrm{d}}{\mathrm{d}\xi}\left(\frac{\partial\mathscr{L}}{\partial\left(\frac{\mathrm{d}^2\tilde{u}}{\mathrm{d}\xi^2}\right)}\right) - \frac{\partial\mathscr{L}}{\partial\left(\frac{\mathrm{d}\tilde{u}}{\mathrm{d}\xi}\right)} = \gamma, \tag{38}$$

with $\gamma \in \mathbb{R}$ being independent of ξ. Multiplying both sides of the previous equation by the factor $\frac{\mathrm{d}^2\tilde{u}}{\mathrm{d}\xi^2}$ gives

$$\frac{\mathrm{d}^2\tilde{u}}{\mathrm{d}\xi^2}\frac{\mathrm{d}}{\mathrm{d}\xi}\left(\frac{\partial\mathscr{L}}{\partial\left(\frac{\mathrm{d}^2\tilde{u}}{\mathrm{d}\xi^2}\right)}\right) - \frac{\mathrm{d}^2\tilde{u}}{\mathrm{d}\xi^2}\left(\frac{\partial\mathscr{L}}{\partial\left(\frac{\mathrm{d}\tilde{u}}{\mathrm{d}\xi}\right)}\right) = \gamma\frac{\mathrm{d}^2\tilde{u}}{\mathrm{d}\xi^2}. \tag{39}$$

The equation above can be rewritten as

$$\frac{\mathrm{d}}{\mathrm{d}\xi}\left[\frac{\mathrm{d}^2\tilde{u}}{\mathrm{d}\xi^2}\left(\frac{\partial\mathscr{L}}{\partial\left(\frac{\mathrm{d}^2\tilde{u}}{\mathrm{d}\xi^2}\right)}\right) - \mathscr{L} - \gamma\frac{\mathrm{d}\tilde{u}}{\mathrm{d}\xi} - \eta\right] = 0, \tag{40}$$

where $\eta \in \mathbb{R}$ is constant with respect to ξ, by noting, owing to the chain rule, that

$$\begin{aligned}\frac{\mathrm{d}}{\mathrm{d}\xi}\left[\frac{\mathrm{d}^2\tilde{u}}{\mathrm{d}\xi^2}\left(\frac{\partial\mathscr{L}}{\partial\left(\frac{\mathrm{d}^2\tilde{u}}{\mathrm{d}\xi^2}\right)}\right) - \mathscr{L} - \gamma\frac{\mathrm{d}\tilde{u}}{\mathrm{d}\xi} - \eta\right] &= \frac{\mathrm{d}^3\tilde{u}}{\mathrm{d}\xi^3}\frac{\partial\mathscr{L}}{\partial\left(\frac{\mathrm{d}^2\tilde{u}}{\mathrm{d}\xi^2}\right)} + \frac{\mathrm{d}^2\tilde{u}}{\mathrm{d}\xi^2}\frac{\mathrm{d}}{\mathrm{d}\xi}\left(\frac{\partial\mathscr{L}}{\partial\left(\frac{\mathrm{d}^2\tilde{u}}{\mathrm{d}\xi^2}\right)}\right) - \frac{\partial\mathscr{L}}{\partial\left(\frac{\mathrm{d}\tilde{u}}{\mathrm{d}\xi}\right)}\frac{\mathrm{d}^2\tilde{u}}{\mathrm{d}\xi^2} - \frac{\partial\mathscr{L}}{\partial\left(\frac{\mathrm{d}^2\tilde{u}}{\mathrm{d}\xi^2}\right)}\frac{\mathrm{d}^3\tilde{u}}{\mathrm{d}\xi^3} - \gamma\frac{\mathrm{d}^2\tilde{u}}{\mathrm{d}\xi^2} \\ &= \frac{\mathrm{d}^2\tilde{u}}{\mathrm{d}\xi^2}\frac{\mathrm{d}}{\mathrm{d}\xi}\left(\frac{\partial\mathscr{L}}{\partial\left(\frac{\mathrm{d}^2\tilde{u}}{\mathrm{d}\xi^2}\right)}\right) - \frac{\mathrm{d}^2\tilde{u}}{\mathrm{d}\xi^2}\left(\frac{\partial\mathscr{L}}{\partial\left(\frac{\mathrm{d}\tilde{u}}{\mathrm{d}\xi}\right)}\right) - \gamma\frac{\mathrm{d}^2\tilde{u}}{\mathrm{d}\xi^2}.\end{aligned}$$

Equation (40), integrating with respect to ξ and performing an abuse of notation, hence becomes

$$\frac{\mathrm{d}^2\tilde{u}}{\mathrm{d}\xi^2}\left(\frac{\partial\mathscr{L}}{\partial\left(\frac{\mathrm{d}^2\tilde{u}}{\mathrm{d}\xi^2}\right)}\right)-\mathscr{L}-\gamma\frac{\mathrm{d}\tilde{u}}{\mathrm{d}\xi}=\eta. \tag{41}$$

where the quantities γ, $\eta\in\mathbb{R}$ are independent of ξ.

Acknowledgments

The author wishes to thank Sergey Gavrilyuk for having introduced him to some of the techniques utilized in the present paper.

The research reported in the present contribution was carried out as part of the project "A Fluid-Structure Interaction tool for the protection of Clean Energy Production sites (FSI-CEP)" funded by the MUR Progetti di Ricerca di Rilevante Interesse Nazionale (PRIN) Bando 2022 PNRR, grant P20227CSJ5.

References

[1] B. E. Abali, W. H. Müller, and V. A. Eremeyev, "Strain gradient elasticity with geometric nonlinearities and its computational evaluation", *Mech. Adv. Mater. Mod. Processes* **1**:1 (2015), art. id. 4.

[2] H. Abdoul-Anziz and P. Seppecher, "Strain gradient and generalized continua obtained by homogenizing frame lattices", *Math. Mech. Complex Syst.* **6**:3 (2018), 213–250.

[3] J.-J. Alibert, P. Seppecher, and F. Dell'Isola, "Truss modular beams with deformation energy depending on higher displacement gradients", *Math. Mech. Solids* **8**:1 (2003), 51–73.

[4] H. Altenbach and V. A. Eremeyev, "On the linear theory of micropolar plates", *Z. Angew. Math. Mech.* **89**:4 (2009), 242–256.

[5] M. N. Arnesen, "Decay and symmetry of solitary waves", *J. Math. Anal. Appl.* **507**:1 (2022), art. id. 125450.

[6] H. Askes and A. R. Wallace, "Dynamic Bergan–Wang theory for thick plates", *Math. Mech. Complex Syst.* **10**:2 (2022), 191–204.

[7] E. Barchiesi, S. R. Eugster, L. Placidi, and F. dell'Isola, "Pantographic beam: a complete second gradient 1D-continuum in plane", *Z. Angew. Math. Phys.* **70**:5 (2019), art. id. 135.

[8] E. Barchiesi, M. Laudato, and F. Di Cosmo, "Wave dispersion in non-linear pantographic beams", *Mech. Res. Commun.* **94** (2018), 128–132.

[9] R. Barretta, M. Čanadija, L. Feo, R. Luciano, F. Marotti de Sciarra, and R. Penna, "Exact solutions of inflected functionally graded nano-beams in integral elasticity", *Compos. B Eng.* **142** (2018), 273–286.

[10] R. Barretta, F. Fabbrocino, R. Luciano, and F. M. d. Sciarra, "Closed-form solutions in stress-driven two-phase integral elasticity for bending of functionally graded nano-beams", *Physica E* **97** (2018), 13–30.

[11] R. Barretta, L. Feo, R. Luciano, F. Marotti de Sciarra, and R. Penna, "Functionally graded Timoshenko nanobeams: a novel nonlocal gradient formulation", *Compos. B Eng.* **100** (2016), 208–219.

[12] A. Berezovski, I. Giorgio, and A. Della Corte, "Interfaces in micromorphic materials: wave transmission and reflection with numerical simulations", *Math. Mech. Solids* **21**:1 (2016), 37–51.

[13] A. Bichara and F. dell'Isola, *Elementi di algebra tensoriale con applicazioni alla meccanica dei solidi*, Società Editrice Esculapio, 2023.

[14] J. C. Bronski, L. D. Carr, B. Deconinck, and J. N. Kutz, "Bose–Einstein condensates in standing waves: the cubic nonlinear Schrödinger equation with a periodic potential", *Phys. Rev. Lett.* **86** (2001), 1402–1405.

[15] J. Chróścielewski, F. dell'Isola, V. A. Eremeyev, and A. Sabik, "On rotational instability within the nonlinear six-parameter shell theory", *Int. J. Solids Struct.* **196–197** (2020), 179–189.

[16] A. Ciallella, F. D'Annibale, D. Del Vescovo, and I. Giorgio, "Deformation patterns in a second-gradient lattice annular plate composed of "Spira mirabilis" fibers", *Contin. Mech. Therm.* **35**:4 (2023), 1561–1580.

[17] A. Ciallella, I. Giorgio, S. R. Eugster, N. L. Rizzi, and F. dell'Isola, "Generalized beam model for the analysis of wave propagation with a symmetric pattern of deformation in planar pantographic sheets", *Wave Motion* **113** (2022), art. id. 102986.

[18] E. N. M. Cirillo, G. Saccomandi, and G. Sciarra, "Compact structures as true non-linear phenomena", *Math. Eng.* **1**:3 (2019), 434–446.

[19] M. De Angelo, E. Barchiesi, I. Giorgio, and B. E. Abali, "Numerical identification of constitutive parameters in reduced-order bi-dimensional models for pantographic structures: application to out-of-plane buckling", *Arch. Appl. Mech.* **89**:7 (2019), 1333–1358.

[20] M. D. Angelo, L. Placidi, N. Nejadsadeghi, and A. Misra, "Non-standard Timoshenko beam model for chiral metamaterial: identification of stiffness parameters", *Mech. Res. Commun.* **103** (2020), art. id. 103462.

[21] J. de Castro Motta, F. Fraternali, and G. Saccomandi, "Rarefaction pulses on tensegrity lattices are just sech^2-solitary (dark) waves", *Meccanica* (*Milano*) **60**:10–11 (2024), 3429–3438.

[22] R. dell'Erba, "Position-based dynamic of a particle system: a configurable algorithm to describe complex behaviour of continuum material starting from swarm robotics", *Contin. Mech. Therm.* **30**:5 (2018), 1069–1090.

[23] R. dell'Erba, "Swarm robotics and complex behaviour of continuum material", *Contin. Mech. Therm.* **31**:4 (2019), 989–1014.

[24] R. dell'Erba, "On how swarm robotics can be used to describe particle system's deformation", *Contin. Mech. Therm.* **34**:4 (2022), 955–975.

[25] R. dell'Erba, "Rules governing swarm robot in continuum mechanics", *Math. Mech. Solids* **27**:10 (2022), 1930–1949.

[26] F. dell'Isola, A. Della Corte, and I. Giorgio, "Higher-gradient continua: the legacy of Piola, Mindlin, Sedov and Toupin and some future research perspectives", *Math. Mech. Solids* **22**:4 (2017), 852–872.

[27] F. dell'Isola, S. R. Eugster, R. Fedele, and P. Seppecher, "Second-gradient continua: from Lagrangian to Eulerian and back", *Math. Mech. Solids* **27**:12 (2022), 2715–2750.

[28] F. dell'Isola, P. Seppecher, J. J. Alibert, T. Lekszycki, R. Grygoruk, M. Pawlikowski, D. Steigmann, I. Giorgio, U. Andreaus, E. Turco, M. Gołaszewski, N. Rizzi, C. Boutin, V. A. Eremeyev, A. Misra, L. Placidi, E. Barchiesi, L. Greco, M. Cuomo, A. Cazzani, A. D. Corte, A. Battista, D. Scerrato, I. Z. Eremeeva, Y. Rahali, J.-F. Ganghoffer, W. Müller, G. Ganzosch, M. Spagnuolo, A. Pfaff, K. Barcz, K. Hoschke, J. Neggers, and F. Hild, "Pantographic metamaterials: an example of mathematically driven design and of its technological challenges", *Contin. Mech. Therm.* **31**:4 (2018), 851–884.

[29] F. dell'Isola, P. Seppecher, M. Spagnuolo, E. Barchiesi, F. Hild, T. Lekszycki, I. Giorgio, L. Placidi, U. Andreaus, M. Cuomo, S. R. Eugster, A. Pfaff, K. Hoschke, R. Langkemper, E. Turco, R. Sarikaya, A. Misra, M. De Angelo, F. D'Annibale, A. Bouterf, X. Pinelli, A. Misra, B. Desmorat, M. Pawlikowski, C. Dupuy, D. Scerrato, P. Peyre, M. Laudato, L. Manzari, P. Göransson, C. Hesch, S. Hesch, P. Franciosi, J. Dirrenberger, F. Maurin, Z. Vangelatos, C. Grigoropoulos, V. Melissinaki, M. Farsari, W. Muller, B. E. Abali, C. Liebold, G. Ganzosch, P. Harrison, R. Drobnicki, L. Igumnov, F. Alzahrani, and T. Hayat, "Advances in pantographic structures: design, manufacturing, models, experiments and image analyses", *Contin. Mech. Therm.* **31**:4 (2019), 1231–1282.

[30] B. Deng, V. Tournat, P. Wang, and K. Bertoldi, "Anomalous collisions of elastic vector solitons in mechanical metamaterials", *Phys. Rev. Lett.* **122**:4 (2019), art. id. 044101.

[31] P. G. Drazin and R. S. Johnson, *Solitons: an introduction*, Cambridge Univ. Press, 1989.

[32] V. A. Eremeyev, F. dell'Isola, C. Boutin, and D. Steigmann, "Linear pantographic sheets: existence and uniqueness of weak solutions", *J. Elasticity* **132**:2 (2018), 175–196.

[33] V. A. Eremeyev and I. Elishakoff, "On rotary inertia of microstuctured beams and variations thereof", *Mech. Res. Commun.* **135** (2024), art. id. 104239.

[34] V. A. Eremeyev and W. Pietraszkiewicz, "Material symmetry group of the non-linear polar-elastic continuum", *Int. J. Solids Struct.* **49**:14 (2012), 1993–2005.

[35] V. A. Eremeyev and W. Pietraszkiewicz, "Material symmetry group and constitutive equations of micropolar anisotropic elastic solids", *Math. Mech. Solids* **21**:2 (2016), 210–221.

[36] V. A. Eremeyev and E. Reccia, "On dynamics of elastic networks with rigid junctions within nonlinear micro-polar elasticity", *Int. J. Multiscale Comput. Eng.* **20**:6 (2022), 1–11.

[37] S. R. Eugster, "Numerical analysis of nonlinear wave propagation in a pantographic sheet", *Math. Mech. Complex Syst.* **9**:3 (2021), 293–310.

[38] S. R. Eugster, F. dell'Isola, R. Fedele, and P. Seppecher, "Piola transformations in second-gradient continua", *Mech. Res. Commun.* **120** (2022), art. id. 103836.

[39] F. Fabbrocino, M. F. Funari, F. Greco, P. Lonetti, R. Luciano, and R. Penna, "Dynamic crack growth based on moving mesh method", *Compos. B Eng.* **174** (2019), art. id. 107053.

[40] R. Fedele, "Third-gradient continua: nonstandard equilibrium equations and selection of work conjugate variables", *Math. Mech. Solids* **27**:10 (2022), 2046–2072.

[41] R. Fedele, "Approach à la Piola for the equilibrium problem of bodies with second gradient energies, II: variational derivation of second gradient equations and their transport", *Contin. Mech. Therm.* **34**:5 (2022), 1087–1111.

[42] R. Fedele, "Piola's approach to the equilibrium problem for bodies with second gradient energies, I: first gradient theory and differential geometry", *Contin. Mech. Therm.* **34**:2 (2022), 445–474.

[43] E. Fermi, P. Pasta, S. Ulam, and M. Tsingou, "Studies of nonlinear problems", technical report, Los Alamos National Laboratory, Los Alamos, NM, 1955.

[44] F. Fraternali, L. Senatore, and C. Daraio, "Solitary waves on tensegrity lattices", *J. Mech. Phys. Solids* **60**:6 (2012), 1137–1144.

[45] M. F. Funari, S. Spadea, F. Fabbrocino, and R. Luciano, "A moving interface finite element formulation to predict dynamic edge debonding in FRP-strengthened concrete beams in service conditions", *Fibers* **8**:6 (2020), art. id. 42.

[46] I. Giorgio, M. De Angelo, E. Turco, and A. Misra, "A Biot–Cosserat two-dimensional elastic nonlinear model for a micromorphic medium", *Contin. Mech. Therm.* **32**:5 (2020), 1357–1369.

[47] I. Giorgio, A. Della Corte, and F. dell'Isola, "Dynamics of 1D nonlinear pantographic continua", *Nonlinear Dyn.* **88**:1 (2016), 21–31.

[48] I. Giorgio, F. dell'Isola, and A. Misra, "Chirality in 2D Cosserat media related to stretch-micro-rotation coupling with links to granular micromechanics", *Int. J. Solids Struct.* **202** (2020), 28–38.

[49] I. Giorgio, P. Harrison, F. dell'Isola, J. Alsayednoor, and E. Turco, "Wrinkling in engineering fabrics: a comparison between two different comprehensive modelling approaches", *Proc. R. Soc. A* **474**:2216 (2018), art. id. 20180063.

[50] C. Guarcello, D. Valenti, A. Carollo, and B. Spagnolo, "Effects of Lévy noise on the dynamics of sine-Gordon solitons in long Josephson junctions", *J. Stat. Mech. Theory Exp.* 5 (2016), art. id. 054012.

[51] A. Javili, F. dell'Isola, and P. Steinmann, "Geometrically nonlinear higher-gradient elasticity with energetic boundaries", *J. Mech. Phys. Solids* **61**:12 (2013), 2381–2401.

[52] D. J. Korteweg and G. de Vries, "On the change of form of long waves advancing in a rectangular canal, and on a new type of long stationary waves", *Philos. Mag.* (5) **39**:240 (1895), 422–443.

[53] G. La Valle, B. E. Abali, G. Falsone, and C. Soize, "Sensitivity of a homogeneous and isotropic second-gradient continuum model for particle-based materials with respect to uncertainties", *Z. Angew. Math. Mech.* **103**:10 (2023), art. id. 202300068.

[54] G. La Valle and C. Soize, "A higher-order nonlocal elasticity continuum model for deterministic and stochastic particle-based materials", *Z. Angew. Math. Phys.* **75**:2 (2024), art. id. 49.

[55] M. Laudato, L. Manzari, I. Giorgio, M. Spagnuolo, and P. Göransson, "Dynamics of pantographic sheet around the clamping region: experimental and numerical analysis", *Math. Mech. Solids* **26**:10 (2021), 1515–1537.

[56] R. Luciano, A. Caporale, H. Darban, and C. Bartolomeo, "Variational approaches for bending and buckling of non-local stress-driven Timoshenko nano-beams for smart materials", *Mech. Res. Commun.* **103** (2020), art. id. 103470.

[57] B. Malomed, "Nonlinear Schrödinger equations", pp. 639–643 in *Encyclopedia of nonlinear science*, edited by A. Scott, Routledge, New York, 2005.

[58] A. Misra and N. Nejadsadeghi, "Longitudinal and transverse elastic waves in 1D granular materials modeled as micromorphic continua", *Wave Motion* **90** (2019), 175–195.

[59] A. Misra, N. Nejadsadeghi, M. De Angelo, and L. Placidi, "Chiral metamaterial predicted by granular micromechanics: verified with 1D example synthesized using additive manufacturing", *Contin. Mech. Therm.* **32**:5 (2020), 1497–1513.

[60] N. Nejadsadeghi and A. Misra, "Role of higher-order inertia in modulating elastic wave dispersion in materials with granular microstructure", *Int. J. Mech. Sci.* **185** (2020), art. id. 105867.

[61] O. Nikan, Z. Avazzadeh, and M. N. Rasoulizadeh, "Soliton solutions of the nonlinear sine-Gordon model with Neumann boundary conditions arising in crystal dislocation theory", *Nonlinear Dyn.* **106**:1 (2021), 783–813.

[62] W. Pietraszkiewicz and V. A. Eremeyev, "On natural strain measures of the non-linear micropolar continuum", *Int. J. Solids Struct.* **46**:3-4 (2009), 774–787.

[63] L. Placidi, U. Andreaus, and I. Giorgio, "Identification of two-dimensional pantographic structure via a linear D4 orthotropic second gradient elastic model", *J. Eng. Math.* **103** (2017), 1–21.

[64] L. Placidi, L. Greco, S. Bucci, E. Turco, and N. L. Rizzi, "A second gradient formulation for a 2D fabric sheet with inextensible fibres", *Z. Angew. Math. Phys.* **67**:5 (2016), art. id. 114.

[65] N. Rezaei, E. Barchiesi, D. Timofeev, C. A. Tran, A. Misra, and L. Placidi, "Solution of a paradox related to the rigid bar pull-out problem in standard elasticity", *Mech. Res. Commun.* **126** (2022), art. id. 104015.

[66] N. Rezaei, M. E. Yildizdag, E. Turco, A. Misra, and L. Placidi, "Strain-gradient finite elasticity solutions to rigid bar pull-out test", *Contin. Mech. Therm.* **36**:3 (2024), 607–617.

[67] I. Semenova, G. Dreiden, A. Samsonov, and A. Porubov, "Strain solitary waves in inhomogeneous wave guides", *Opt. Lasers Eng.* **34**:3 (2000), 159–168.

[68] V. Settimi, M. Lepidi, and A. Bacigalupo, "Nonlinear dispersion properties of one-dimensional mechanical metamaterials with inertia amplification", *Int. J. Mech. Sci.* **201** (2021), art. id. 106461.

[69] N. Shekarchizadeh, B. E. Abali, E. Barchiesi, and A. M. Bersani, "Inverse analysis of metamaterials and parameter determination by means of an automatized optimization problem", *Z. Angew. Math. Mech.* **101**:8 (2021), art. id. 202000277.

[70] E. Turco and E. Barchiesi, "Kinematically triggered nonlinear vibrations of Hencky-type pantographic sheets", *Math. Mech. Complex Syst.* **9**:3 (2021), 311–335.

[71] E. Turco, E. Barchiesi, A. Ciallella, and F. dell'Isola, "Nonlinear waves in pantographic beams induced by transverse impulses", *Wave Motion* **115** (2022), art. id. 103064.

[72] E. Turco, E. Barchiesi, and F. dell'Isola, "In-plane dynamic buckling of duoskelion beam-like structures: discrete modeling and numerical results", *Math. Mech. Solids* **27**:7 (2022), 1164–1184.

[73] E. Turco, E. Barchiesi, and F. dell'Isola, "A numerical investigation on impulse-induced nonlinear longitudinal waves in pantographic beams", *Math. Mech. Solids* **27**:1 (2022), 22–48.

[74] N. Vaiana, S. Sessa, F. Marmo, and L. Rosati, "A class of uniaxial phenomenological models for simulating hysteretic phenomena in rate-independent mechanical systems and materials", *Nonlinear Dyn.* **93**:3 (2018), 1647–1669.

[75] H. Yang, B. E. Abali, W. H. Müller, S. Barboura, and J. Li, "Verification of asymptotic homogenization method developed for periodic architected materials in strain gradient continuum", *Int. J. Solids Struct.* **238** (2022), art. id. 111386.

[76] H. Yang, G. Ganzosch, I. Giorgio, and B. E. Abali, "Material characterization and computations of a polymeric metamaterial with a pantographic substructure", *Z. Angew. Math. Phys.* **69**:4 (2018), art. id. 105.

[77] N. J. Zabusky and M. D. Kruskal, "Interaction of "solitons" in a collisionless plasma and the recurrence of initial states", *Phys. Rev. Lett.* **15**:6 (1965), 240–243.

Received 7 May 2025. Revised 14 Nov 2025. Accepted 7 Dec 2025.

EMILIO BARCHIESI: ebarchiesi@uniss.it
Dipartimento di Architettura, design e urbanistica, Università degli Studi di Sassari, Alghero, Italy

and

Centro Internazionale di Ricerca M&MoCS, Università degli Studi dell'Aquila, L'Aquila, Italy